



Exploring the Mass and Redshift Dependencies of the Cluster Pressure Profile with Stacks on Thermal Sunyaev–Zel’dovich Maps

Denis Tramonte^{1,2,3,4} , Yin-Zhe Ma^{3,4,5,1} , Ziang Yan^{6,7} , Matteo Maturi^{8,9} , Gianluca Castignani^{10,11} ,
Mauro Sereno^{11,12} , Sandro Bardelli¹¹ , Carlo Giocoli^{11,10,12} , Federico Marulli^{10,11,12} , Lauro Moscardini^{10,11,12} ,

Emanuela Puddu¹³ , Mario Radovich¹⁴ , Ludovic Van Waerbeke⁷ , and Angus H. Wright⁶

¹ Purple Mountain Observatory, No. 8 Yuanhua Road, Qixia District, Nanjing 210034, People’s Republic of China; Denis.Tramonte@xjtu.edu.cn

² Department of Physics, Xi’an Jiaotong-Liverpool University, 111 Ren’ai Road, Suzhou Dushu Lake Science and Education Innovation District, Suzhou Industrial Park, Suzhou 215123, People’s Republic of China

³ NAOC-UKZN Computational Astrophysics Center (NUCAC), University of KwaZulu-Natal, Durban, 4000, South Africa; ma@ukzn.ac.za

⁴ School of Chemistry and Physics, University of KwaZulu-Natal, Westville Campus, Private Bag X54001, Durban, South Africa

⁵ National Institute for Theoretical and Computational Sciences (NITheCS), South Africa

⁶ Ruhr University Bochum, Faculty of Physics and Astronomy, Astronomical Institute (AIRUB), German Centre for Cosmological Lensing, D-44780 Bochum, Germany

⁷ Department of Physics and Astronomy, University of British Columbia, 6224 Agricultural Road, Vancouver, BC, V6T 1Z1, Canada

⁸ Center for Astronomy—University of Heidelberg, Albert-Ueberle-Straße 2, D-69120 Heidelberg, Germany

⁹ Institute of Theoretical Physics—University of Heidelberg, Albert-Ueberle-Straße 2, D-69120 Heidelberg, Germany

¹⁰ Department of Physics and Astronomy “A. Righi” – Alma Mater Studiorum, University of Bologna, Via Piero Gobetti 93/2, I-40129 Bologna, Italy

¹¹ INAF—Astrophysics and Space Science Observatory of Bologna, Via Piero Gobetti 93/3, I-40129 Bologna, Italy

¹² INFN—Bologna Section, Viale Berti Pichat 6/2, I-40127 Bologna, Italy

¹³ INAF—Osservatorio Astronomico di Capodimonte, Salita Moiariello 16, I-80131, Napoli, Italy

¹⁴ INAF—Padua Astronomical Observatory, Vicolo dell’Osservatorio, 5, I-35122 Padova, Italy

Received 2022 September 15; revised 2022 December 7; accepted 2023 February 11; published 2023 April 6

Abstract

We provide novel constraints on the parameters defining the universal pressure profile (UPP) within clusters of galaxies, and explore their dependencies on cluster mass and redshift, from measurements of Sunyaev–Zel’dovich (SZ) Compton y -profiles. We employ both Planck 2015 MILCA and Atacama Cosmology Telescope (ACT) Data Release 4 y -maps over a common $\sim 2100 \text{ deg}^2$ footprint. We combine existing cluster catalogs, based on Kilo Degree Survey, Sloan Digital Sky Survey, and Dark Energy Spectroscopic Instrument Legacy Imaging Surveys observations, for a total of 23,820 clusters, spanning the mass range $10^{14.0} M_{\odot} < M_{500} < 10^{15.1} M_{\odot}$ and the redshift range $0.02 < z < 0.98$. We split the clusters into three independent bins in mass and redshift; for each combination, we detect the stacked SZ cluster signal and extract the mean y angular profile. The latter is predicted theoretically by adopting a halo model framework, and a Markov Chain Monte Carlo approach is employed to estimate the UPP parameters, the hydrostatic mass bias b_h , and possible cluster miscentering effects. We constrain $[P_0, c_{500}, \alpha, \beta]$ to $[5.9, 2.0, 1.8, 4.9]$ with Planck and to $[3.8, 1.3, 1.0, 4.4]$ with ACT, using the full cluster sample, in agreement with previous findings. We do not find any compelling evidence for residual mass or redshift dependencies, thus expanding the validity of the cluster pressure profile over much larger M_{500} and z ranges; this is the first time that the model has been tested on such a large (complete and representative) cluster sample. Finally, we obtain loose constraints on the hydrostatic mass bias in the range 0.2–0.3, again in broad agreement with previous works.

Unified Astronomy Thesaurus concepts: Galaxy clusters (584); Intracluster medium (858); Large-scale structure of the universe (902)

1. Introduction

Galaxy clusters are invaluable cosmological probes, providing information about the geometry of the universe, about the growths of cosmic structures, and, at lower scales, about the processes of galaxy formation and evolution (Voit 2005; Allen et al. 2011). The majority of cluster baryonic matter (up to 90%) is found as a diffuse component referred to as the intracluster medium (ICM), which is shock heated and ionized in the strong cluster gravitational field, up to temperatures of 5–10 keV. A proper characterization of the physical properties of the ICM is of great interest, not only for allowing indirect calibrations of the mass proxies based on ICM observations, but also for providing useful insights into the processes of galaxy evolution and feedback.

The high temperature of the ICM plasma has made it a traditional target for X-ray observations (Sarazin 1988), a property that has been exploited by different generations of satellite missions to build X-ray cluster catalogs (Voges et al. 1999; Hicks et al. 2008; Mehrrens et al. 2012; Klein et al. 2022). A complementary probe is the observation of the thermal Sunyaev–Zel’dovich (tSZ) effect (Sunyaev & Zeldovich 1972), a secondary anisotropy of the cosmic microwave background (CMB) radiation that is produced when CMB photons interact with a population of high-energy electrons via inverse Compton scattering. The resulting temperature fluctuations with respect to the CMB temperature T_{CMB} can be expressed as

$$\frac{\Delta T}{T_{\text{CMB}}} = f(\xi)y, \quad (1)$$

where the dependence on the scaled frequency $\xi \equiv h\nu/(k_{\text{B}} T_{\text{CMB}})$, with h and k_{B} being the Planck and Boltzmann

Table 1
Summary of Previous Estimates of the Parameters Entering the UPP Expression in Equation (3)

Reference	Data Set		UPP Parameters				
	Objects	Observables	P_0	c_{500}	α	β	γ
Nagai et al. (2007)	16 clusters	X-ray, simulations	3.3	1.8	1.3	4.3	0.7
Arnaud et al. (2010)	33 clusters	X-ray, simulations	$8.403 h_{70}^{-3/2}$	1.177	1.0510	5.4905	0.3081
Planck Collaboration et al. (2013)	62 clusters	SZ, X-ray	6.41	1.81	1.33	4.13	0.31
Sayers et al. (2016)	47 clusters	SZ, X-ray	9.13 ± 2.98	1.18	1.0510	6.13 ± 0.76	0.3081
Gong et al. (2019)	$\sim 10^5$ LRGs	SZ	$2.18^{+9.02}_{-1.98}$	$1.05^{+1.27}_{-0.47}$	$1.52^{+1.47}_{-0.58}$	$3.91^{+0.87}_{-0.44}$	0.31
Ma et al. (2021)	...	SZ, WL (convergence)	$9.68^{+10.02}_{-7.11}$	$2.71^{+0.92}_{-0.93}$	$5.97^{+1.81}_{-4.73}$	$3.47^{+1.39}_{-0.60}$	0.31
Ma et al. (2021)	...	SZ, WL (shear)	$6.62^{+2.06}_{-1.65}$	$1.91^{+1.07}_{-0.65}$	$1.65^{+0.74}_{-0.50}$	$4.88^{+1.18}_{-2.46}$	0.31
Pointecouteau et al. (2021)	31 clusters	SZ	$3.36^{+0.90}_{-0.71}$	1.18	$1.08^{+0.13}_{-0.11}$	4.30 ± 0.12	0.31
He et al. (2021)	33 clusters	X-ray, simulations	5.048	1.217	1.192	5.490	0.433

Note. For each work, we report the reference in the literature, the number of clusters used in the study (when applicable), the physical observables used, and the best-fit values for the UPP parameters. The boldface values remained fixed in the corresponding fits. For more details, we redirect the reader to Appendix A.

constants, is encoded in the function $f(\xi) = \xi \coth(\xi/2) - 4$; the result is a decrease (increase) in the CMB temperature at frequencies below (above) 217 GHz. The magnitude of the effect is quantified by the Compton parameter y , which is proportional to the electron pressure integrated along the line of sight (LoS):

$$y = \frac{\sigma_T}{m_e c^2} \int_{\text{LoS}} dl P_e(l), \quad (2)$$

where σ_T is the Thomson cross section, $m_e c^2$ is the electron rest energy, and $P_e(l)$ is the electron pressure at a physical LoS separation l .

The high-energy electrons found in the ICM make the tSZ effect an ideal probe for detecting and studying galaxy clusters (Birkinshaw 1999; Carlstrom et al. 2002). Unlike the X-ray brightness, which is proportional to the squared electron density n_e^2 , the Compton parameter is proportional to n_e , which implies that it has a higher sensitivity to low-mass densities and can be used to trace the ICM out to larger separations from the cluster core. In addition, it is independent of the cluster redshift,¹⁵ and tSZ observations can conveniently be carried out at radio and microwave frequencies from ground-based observatories. The advances in tSZ observational techniques over the past two decades have yielded dedicated tSZ-detected cluster catalogs as well as the reconstruction of the Compton parameter signal over extended areas of the sky, using both satellite missions, like Planck (Planck Collaboration et al. 2016a), and ground-based facilities, like the Atacama Cosmology Telescope (ACT; Hilton et al. 2021) and the South Pole Telescope (Bleem et al. 2020).

In the case of both X-ray and tSZ data, the proper characterization of the ICM eventually translates into the modeling of the local electron pressure. The analysis presented in Nagai et al. (2007) first proposed a generalized Navarro–Frenk–White (NFW; Navarro et al. 1997) parameterization as a

universal model for the electron pressure profile, in the form

$$\mathbb{P}(x) \equiv \frac{P_e(r)}{P_{500}} = \frac{P_0}{(c_{500}x)^\gamma [1 + (c_{500}x)^\alpha]^{(\beta-\gamma)/\alpha}}, \quad (3)$$

where $P_e(r)$ is the electron pressure at a physical separation r from the cluster center and P_{500} is the characteristic pressure expected in a self-similar model (Section 5.1), carrying the dependence on the cluster mass and redshift, with the profile being expressed as a function of the scaled radial separation¹⁶ $x \equiv r/R_{500}$. This universal pressure profile (UPP) is parameterized in terms of the concentration¹⁷ c_{500} , an overall normalization factor P_0 , and the parameters γ , α , and β , which are, respectively, the profile slopes at small ($x \ll 1/c_{500}$), intermediate ($x \sim 1/c_{500}$), and large ($x \gg 1/c_{500}$) separations from the cluster center. Nagai et al. (2007) provided best-fit estimates for the parameters based on profiles that were reconstructed from Chandra data and results from hydrodynamical simulations.

Over the past decade, several other works have contributed to constraining the UPP parameters, using different observables and techniques. A summary of the results for the fitted UPP parameters from these works is presented in Table 1, while for a more comprehensive summary, we redirect the reader to Appendix A. Most of these studies have employed a limited set of well-characterized and high-significance clusters in order to measure the cluster pressure profile (Arnaud et al. 2010; Planck Collaboration et al. 2013; Sayers et al. 2016; He et al. 2021; Pointecouteau et al. 2021). A substantially different approach was adopted in Gong et al. (2019; hereafter, G19), with the UPP parameters being fitted over a stack of a large number ($\sim 10^5$) of regions surrounding luminous red galaxies (LRGs) at $z \lesssim 0.5$, assuming the latter to be good tracers of massive dark matter halos. This type of work forgoes the profile reconstruction for individual objects, focusing instead on the mean ICM properties of an extended sample. The results were in

¹⁵ Strictly speaking, tSZ observations detect the cluster signal integrated over the beam solid angle Y_{SZ} , which is proportional to the temperature-weighted mass of the cluster $M \langle T_e \rangle$ and to the inverse square of the angular diameter distance at the cluster redshift, $Y_{\text{SZ}} \propto M \langle T_e \rangle D_A(z)^{-2}$ (Carlstrom et al. 2002). This introduces a marginal redshift dependence. In fact, tSZ detections of clusters at $z > 1$ are not common, possibly due to lower ICM temperatures or contamination from radio-loud active galactic nuclei.

¹⁶ Unless explicitly stated, it is understood that overdensity masses and radii refer to the universe’s critical density $\rho_c(z)$ at the considered redshift; in formulae, $M_\Delta = 4\pi \Delta \rho_c(z) R_\Delta^3/3$, with Δ being the overdensity value.

¹⁷ In some work, the UPP is expressed as a function of $x' = r/r_s$, where the scale radius r_s is related to the overdensity radius R_{500} , via the concentration parameter, $c_{500} = R_{500}/r_s$.

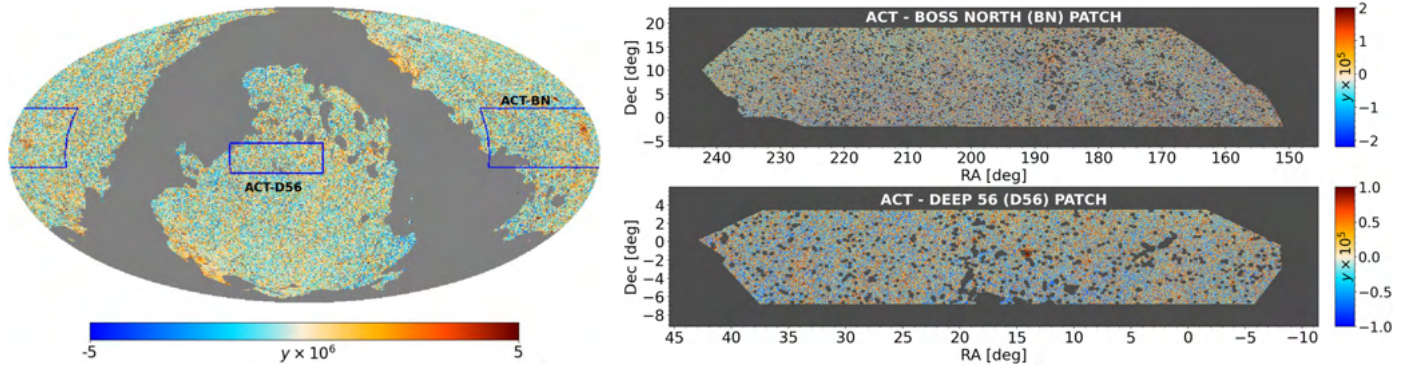


Figure 1. Left: the all-sky Planck 2015 MILCA Compton y -map, plotted in equatorial coordinates, with the Galactic plane 40% mask and the point-source mask being overlaid; the positions of the two ACT patches are also marked by blue boxes. Right: the two patches of the ACT Data Release 4 y -map, combined with the local projection of the mask adopted for Planck. The color scale units are different in Planck and ACT, to better show the features in the corresponding maps; in both cases, the masked regions are shown in gray color.

agreement with those from previous studies, thus proving the feasibility of this approach for characterizing the UPP. Besides, the large number statistics provided by the sample in G19 allowed the authors to split the LRG sample into three redshift bins, finding hints of a redshift evolution of the UPP parameters; the inclusion of an explicit redshift dependence in the normalization pressure P_{500} proved effective in improving the reduced χ^2 when fitting the combination of the three redshift bins. Finally, other more indirect estimates of the UPP parameters were obtained from the cross-correlation between tSZ and weak-lensing (WL) data (Hojjati et al. 2015, 2017; Ma et al. 2021).

The present study aims to extend this line of work by providing novel estimates of the UPP parameters. Our analysis is based on cluster stacks on y -maps; the UPP parameters are then fitted on the reconstructed mean y -profiles. The main difference from G19 is that we use a real cluster catalog, instead of reverting to LRGs as positional tracers. Besides, we also use a complete cluster sample; this is a major difference compared to the cluster-based studies listed in Table 1, whose high-significance cluster samples were incomplete and even, in some cases, nonrepresentative (see Appendix A for a more extensive discussion). Our sample is obtained by merging existing cluster catalogs, yielding a total of $\sim 2.3 \times 10^4$ clusters spanning the M_{500} mass range $[10^{14}, 10^{15.1}] M_{\odot}$ and the photometric redshift range $[0.1, 0.8]$. This is another important difference compared to the analysis in G19, which mostly targeted the mass range of rich groups ($M_{500} \lesssim 10^{14} M_{\odot}$). Furthermore, our large sample allows us to split the data set not only into different redshift bins, but also into different mass bins, thus exploring in greater detail possible deviations from the universality of the pressure profile. Finally, we obtain independent results from both the Planck and ACT Compton maps for the same cluster sample.

This paper is organized as follows. We begin by describing the two data sets employed in our analysis, namely the Compton y -maps (Section 2) and the cluster catalogs (Section 3). Section 4 presents the methodology that we adopt for generating our reference sample, stacking the clusters, and extracting the associated angular y -profiles with their uncertainties. The formalism that we employ to model the cluster y -signal is detailed in Section 5, while the parameter estimation analysis is presented in Section 6. Finally, Section 7 reports the conclusions. Throughout this paper, we adopt a spatially flat Λ CDM cosmological model, with parameter values $h = 0.674$,

$\Omega_m = 0.315$, $\Omega_b = 0.0493$, $\sigma_8 = 0.811$, and $n_s = 0.965$ (Planck Collaboration et al. 2020).

2. Compton Parameter Maps

In this work, we conduct the stacking analysis on two different Compton parameter maps, obtained by Planck and ACT, respectively. We describe each in detail in the following subsections.

2.1. Planck Data

We employ the all-sky Compton parameter map delivered by the Planck Collaboration and described in Planck Collaboration et al. (2016b). The map is publicly available at the Planck Legacy Archive,¹⁸ and it can be downloaded in HEALPix format (Górski et al. 2005), with the pixelization being set by the resolution parameter $N_{\text{side}} = 2048$ (corresponding to a pixel size of $\sim 1'.8$). The map was generated via a tailored linear combination of Planck individual frequency maps. Two versions of the map are available, obtained from two different implementations of the Internal Linear Combination (ILC) algorithm, namely the Modified Internal Linear Combination Algorithm (MILCA; Hurier et al. 2013) and the Needlet Independent Linear Combination (NILC; Remazeilles et al. 2011) methods. In the following, we adopt the MILCA map only, as we have verified that the use of the NILC map yields results for the Compton parameter profiles that are compatible within the final error bars. Prior to their linear combination, the Planck channel maps were first degraded to a common resolution of $10'$, which is the reference FWHM value for the final Compton map.

We adopt a suitable mask to avoid contamination from residual Galactic foregrounds and strong extragalactic radio sources. The Planck Legacy Archive provides a point-source mask and different Galactic masks that are tailored to the tSZ analysis. We combine the 40% Galactic plane mask and the point-source mask, excluding a total of 50.6% of the sky. The Planck MILCA Compton map, combined with our adopted mask, is shown in the first panel of Figure 1.

¹⁸ <https://pla.esac.esa.int/#maps>

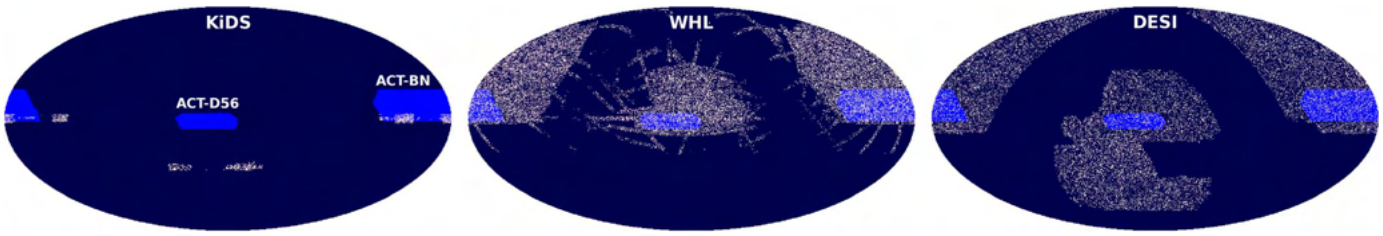


Figure 2. Footprint of the two ACT patches (lighter blue), adopting the same equatorial frame as in the first panel of Figure 1, compared with the angular distributions of our chosen cluster catalogs (white), namely KiDS (left), WHL (middle), and DESI (right).

2.2. ACT Data

We employ the ACT Compton y -map described in Madhavacheril et al. (2020), which is publicly accessible from the LAMBDA website.¹⁹ This map was also built with an ILC approach, using Planck individual frequency maps²⁰ up to 545 GHz and ACT maps at 98 and 150 GHz. The two experiments are complementary in terms of their angular sensitivity: although ACT has higher resolution than Planck and provides superior-quality data at small scales, the Planck large-scale data are free from the atmospheric noise affecting the ACT maps. The limited available sky area, of $\sim 2100 \text{ deg}^2$, allowed the authors to apply an ILC implementation that was tailored to a projected 2D analysis, which is a novel approach compared to previous spherical harmonics-based approaches to analyzing all-sky data. The final map covers two disjoint patches in the sky, labeled as BOSS North (BN; covering 1633 deg^2) and Deep 56 (D56; covering 456 deg^2), for which deep observational ACT data from 2014 and 2015 were available. Unlike the Planck maps, the ACT maps for these patches are provided as 2D arrays in a plate carrée (equirectangular) projection, with a pixel size of ~ 0.5 . The resolution of these ACT maps is $\text{FWHM} = 1'.6$.

Although the individual frequency maps underwent a process of source subtraction prior to their combination, possible residuals are still present in the final product. As no specific point-source mask is available for the ACT tSZ maps, we revert to using the same combined Galactic and point-source Planck mask for these maps as well, by projecting it onto the plane areas covered by ACT.²¹ The resulting masked maps are plotted in the two right panels of Figure 1.

3. Cluster Catalogs

We consider a composite cluster sample that was obtained by merging three independent catalogs, which are individually described in the following sections. The methodology that we adopt for their combination is addressed in Sections 3.4 and 3.5. Note that, in the end, we only consider clusters with mass $M_{500} > 10^{14} M_{\odot}$, as lower masses would not yield significant detections in the stacks, as described in Section 4.2.

¹⁹ https://lambda.gsfc.nasa.gov/product/act/act_dr4_derived_maps_get.cfm

²⁰ Hence, the Planck and ACT tSZ maps are not completely independent. This is not an issue in our study, however, as the choice to use both data sets was made to better exploit all the available tSZ data. In the end, the higher resolution of ACT is still the main factor that makes a difference to the resulting angular Compton profiles.

²¹ Although this mask may potentially miss some point sources entering the ACT footprint, it can be considered conservative, as the larger Planck beam size would result in larger masked areas around each compact source. We also explicitly tested the use of no mask at all, confirming that negligible variations in the ACT profiles presented in Figure 10 are produced, thus proving that the specific masking strategy is not a critical issue in a stacking analysis like the one presented in this paper.

3.1. AMICO–KiDS-DR3 Catalog

We employ the cluster catalog described in Maturi et al. (2019), which was obtained by running the Adaptive Matched Identifier of Clustered Objects (AMICO) algorithm (Bellagamba et al. 2018) on the third data release of the Kilo Degree Survey (KiDS-DR3; de Jong et al. 2017). The KiDS-DR3 data provide photometric redshifts for ~ 48.7 million sources over 447 deg^2 . AMICO is based on a linear optimal matched filter, which (in this particular application) exploits information about galaxy positions, r -band magnitudes, and redshift distributions, to build a 3D map of the amplitude A over the volume spanned by the galaxy catalog. The quantity A , which is evaluated with its associated variance σ_A , is related to the likelihood of finding a galaxy cluster; the location with the highest likelihood is then identified as the first cluster candidate. The signal associated with the latter is subsequently removed from the A map, before the likelihood is reevaluated and the second cluster candidate is searched for. The process is repeated until a low-limit signal-to-noise ratio (S/N) $A/\sigma_A = 3$ is reached; the final output catalog contains 12,939 clusters that are identified with $S/N > 3$, over the redshift range $0.078 < z < 0.754$. We restrict our analysis to the 7957 clusters with $S/N > 3.5$; the resulting sample has a typical $\gtrsim 95\%$ purity over the whole redshift range and a completeness $\gtrsim 90\%$ for $M_{500} > 10^{14} M_{\odot}$ at $z < 0.6$ (Maturi et al. 2019).

The measured amplitude A served as the primary mass proxy for each detection; cluster masses were assigned on the basis of an $A - M_{200}$ scaling relation, where the baseline mean values for the overdensity mass M_{200} were computed from KiDS lensing data (Bellagamba et al. 2019). As it is customary to employ M_{500} as the mass definition in tSZ studies, we convert the AMICO masses into M_{500} , assuming an NFW profile and using the concentration model from Ishiyama et al. (2021). For each cluster, we also generate a population of 200 random values of masses, normally distributed around the M_{200} value and with a dispersion set by the available uncertainty $\sigma_{M_{200}}$; we convert each of these values to M_{500} and adopt their rms as our estimate for the uncertainty $\sigma_{M_{500}}$. The resulting mean uncertainty on $\log_{10}(M_{500}/M_{\odot})$ for the KiDS clusters is 0.194 dex. When queried to match the ACT footprint, the KiDS catalog contributes 3318 clusters (806 clusters with $M_{500} > 10^{14} M_{\odot}$), all located in the ACT–BN patch (Figure 2, left panel).

3.2. SDSS-DR12 WHL Catalog

The catalog described in Wen et al. (2012) identified 132,684 galaxy clusters based on photometric data from the eighth data release of the Sloan Digital Sky Survey (SDSS-DR8; Aihara et al. 2011) in the redshift range $0.05 \leq z < 0.80$. The catalog has a $\gtrsim 94\%$ purity over the whole sample and a $\gtrsim 95\%$ completeness for clusters with $M_{200} > 10^{14} M_{\odot}$ at

$z < 0.42$; the cluster masses were estimated based on their richness and optical luminosity. A more recent update of the catalog, based on the 12th data release of SDSS (DR12; Alam et al. 2015), is presented in Wen & Han (2015); hereafter, we shall label this catalog the WHL catalog.²² The update not only takes advantage of the improved SDSS data quality, providing additional spectroscopic redshift information for a total of ~ 2.3 million galaxies, as well as allowing the cluster detection at high redshifts to be improved, but it also exploits a better-defined mass proxy. The new catalog includes 25,419 additional clusters detected around bright galaxies at high redshift, and it provides updated redshift and richness estimates for the previously identified objects. Each cluster's position is defined by the coordinates of its brightest cluster galaxy, and its redshift is estimated as the mean of the spectroscopic redshifts of the member galaxies (when available). As for the mass estimation, the analysis first defined a calibration sample, by merging the existing cluster samples with mass proxies based on X-ray data (Vikhlinin et al. 2009; Mantz et al. 2010; Piffaretti et al. 2011; Takey et al. 2014) or tSZ data (Hasselfield et al. 2013; Planck Collaboration et al. 2016a). The common clusters across the different catalogs were used to yield a homogeneous mass definition throughout the composite sample, by scaling it to the definition adopted in Vikhlinin et al. (2009). The final calibration sample consisted of 1191 clusters overlapping with the available SDSS data, with mass²³ $M_{500} > 0.3 \times 10^{14} M_{\odot}$ and redshift $0.05 < z < 0.75$. For these clusters, the total r -band luminosity within R_{500} , corrected by a redshift-dependent factor, was found to be well correlated with the cluster mass M_{500} , with a scatter of 0.17 dex. The associated scaling relation can be applied to estimate the masses of all the clusters in the updated WHL catalog.

For our analysis, we employ the updated WHL catalog, with a total of 158,103 clusters spanning the mass range $M_{500} \in [10^{12.3}, 10^{15.5}] M_{\odot}$ and the redshift range $[0.03, 0.80]$, about 77% of which have spectroscopic redshift information. As no mass error estimates are available for the individual clusters, we evaluate a mean uncertainty on M_{500} as follows. We consider the clusters in the calibration sample and convert their measured richness into mass $M_{500}^{(\text{scal})}$, adopting the same scaling relation that is employed in Wen & Han (2015) to compute the mass estimates for the updated cluster catalog. For the calibration sample clusters, the independent mass estimate $M_{500}^{(\text{lit})}$ from the literature is also available;²⁴ we then consider the scatter values $M_{500}^{(\text{scal})} - M_{500}^{(\text{lit})}$ for the calibration clusters and take their rms as the common mass uncertainty for the WHL catalog that we use in our analysis. The result is an uncertainty of 0.187 dex in $\log_{10}(M_{500}/M_{\odot})$, which is slightly more conservative than the value quoted for the scatter of the scaling relation in Wen & Han (2015). The query for matching the ACT footprints yields 27,367 clusters, with 20,967 in the BN patch and 6400 in the D56 patch (Figure 2, central panel); after applying the mass cut $M_{500} > 10^{14} M_{\odot}$, the numbers are 18,597, 14,186, and 4411, respectively.

²² This acronym refers to the initials of the authors of the original publication (Wen et al. 2012). The catalog is publicly available at <https://vizier.u-strasbg.fr/viz-bin/VizieR?source=J/ApJ/807/178>.

²³ In contrast to Wen et al. (2012), where masses are quoted as M_{200} , the work presented in Wen & Han (2015) adopts the M_{500} definition.

²⁴ These mass estimates $M_{500}^{(\text{lit})}$ are the ones obtained from the aforementioned list of X-ray and tSZ studies, following the rescaling that was performed by Wen & Han (2015) to homogenize the mass definition in the calibration sample.

3.3. DESI-DR8 Catalog

This cluster catalog was obtained directly from the galaxy samples in the DESI Legacy Imaging Surveys (Dey et al. 2019) Data Release 8 (DESI-DR8). The catalog's production is described in Yang et al. (2021), and it is based on the updated version of the halo-based group/cluster finder that was presented in Yang et al. (2005) and later employed in Yang et al. (2007). In this case, the cluster mass is computed based on the measured cluster luminosity. The group finder follows an iterative approach: at each stage, the cumulative group luminosity distribution is computed from the known luminosities of the member galaxies; abundance matching with the cumulative halo mass function then allows a tentative mass to be assigned to each group, which, in turn, allows the membership information to be updated. The process starts by assuming that each galaxy is a group candidate, continuing until convergence in the galaxy membership information and the derived mass-to-luminosity ratios. In this case, the estimated mass is defined for an overdensity $\Delta = 180$, with respect to the mean matter density of the universe at the cluster redshift ($M_{180,m}$), while the cluster position is assigned to its geometrical luminosity-weighted center. The authors first tested this halo finder on a mock galaxy catalog generated from the ELUCID simulation (Wang et al. 2016), comparing the results with the output of a traditional Friend-of-Friends algorithm (Davis et al. 1985): in $\sim 90\%$ of groups with mass $M_{180,m} \gtrsim 10^{12.5} h^{-1} M_{\odot}$, the halo finder correctly identified more than 60% of the member galaxies, with a quoted mean mass uncertainty of 0.2 dex for masses $M_{180,m} \gtrsim 10^{13.5} h^{-1} M_{\odot}$; the resulting purity was $>90\%$ for groups with mass $M_{180,m} \gtrsim 10^{12} h^{-1} M_{\odot}$, reaching $\sim 100\%$ for $M_{180,m} \gtrsim 10^{14.5} h^{-1} M_{\odot}$.

The authors subsequently applied the group finder to DESI-DR8, to yield the positions, redshifts, and masses for ~ 92 million objects, the majority of which were low-mass groups with less than three member galaxies. For the purpose of the present analysis, we clearly restrict the sample to the most massive objects; after converting the mass to the M_{500} definition with the concentration model from Ishiyama et al. (2021), we apply the mass cut $M_{500} > 10^{14} M_{\odot}$, resulting in a total of 110,908 objects spanning the redshift range $z \in [0.02, 0.97]$. Given our low mass cut, and the lack of error estimates on individual cluster masses, we can adopt the quoted value 0.2 dex as the common uncertainty on $\log_{10}(M_{500}/M_{\odot})$. We find 13,018 clusters overlapping with the ACT maps, with 10,253 in the BN patch and 2765 in the D56 patch (Figure 2, right panel).

3.4. Mass Calibration

With the aim of employing the largest possible statistics in our study of the cluster pressure profile, we merge the three catalogs described above together. In order to avoid potential biases in the subsequent analysis, care needs to be taken in this operation to ensure that the cluster mass definition is consistent across all the catalogs that we combine. Although we adopt the M_{500} definition in every case, the masses from the different catalogs are based on different observables, scaling relations, and methodologies.

We then search for cluster matches between pairs of catalogs and compare the associated mass values. Our matching criterion is purely positional: two clusters in different catalogs are considered to be the same object if their projected linear separation on the sky Δr and their redshift separation Δz

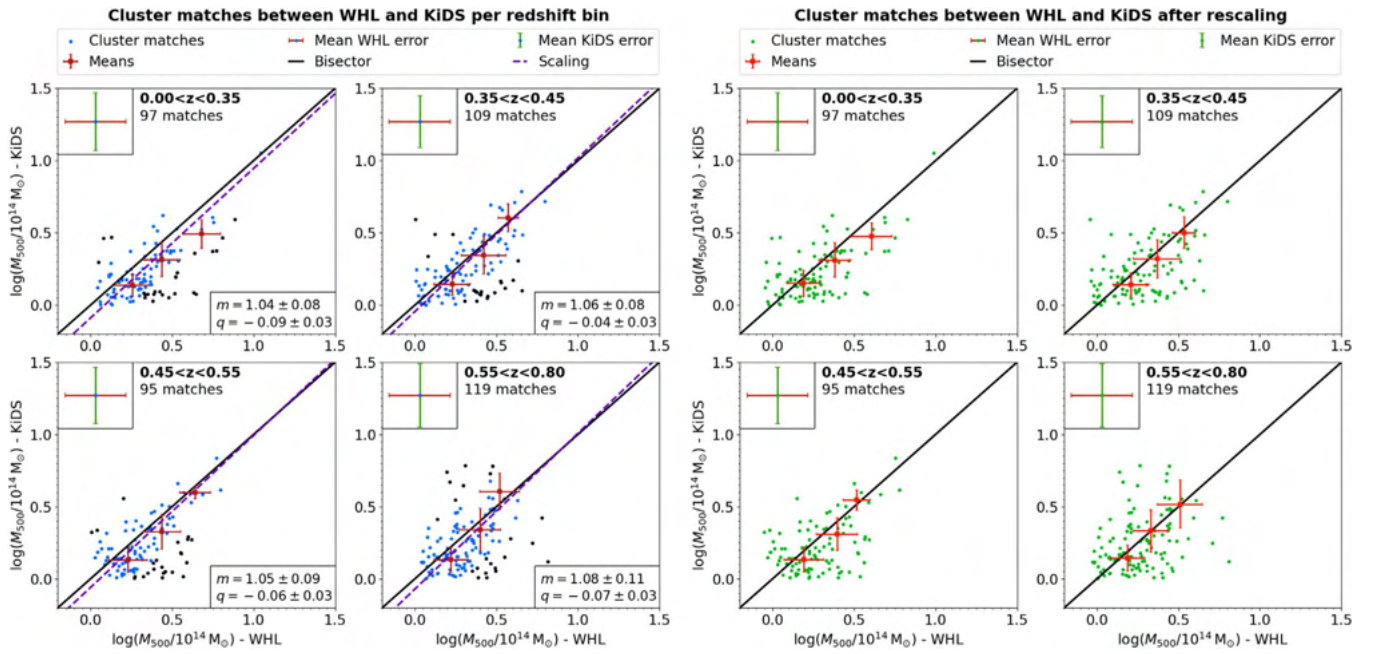


Figure 3. Summary of the mass calibration analysis described in Section 3.4, for the KiDS–WHL comparison. Left panels: for each redshift bin, we plot a comparison between the masses for the retrieved cluster matches from the two catalogs using dots; the bisector $y = x$ is shown for comparison, as a solid black line. The mean error bars for the mass estimates for each match are shown in separate boxes in the top left corners. The red squares and their error bars represent the means and standard deviations of the masses of the matches binned along the bisector, and serve to better visualize the trend of the points compared to the bisector. The dashed purple line represents the linear regression adopted to scale the WHL masses to the KiDS masses, according to Equation (4), with the scaling parameters quoted in the bottom right corners of each plot; the matches that are plotted in black were considered outliers and were not included in the linear fit. Right panels: the same as the left panels, but after applying the rescaling to the WHL masses; overall, the scaling improves the agreement between the masses of the matched clusters.

satisfy the conditions $\Delta r < 0.5 \text{ Mpc}$ and $\Delta z < 0.05(1 + \bar{z})$, where \bar{z} is the mean redshift of the two clusters (this expression for the limit on Δz takes into account the potentially higher errors on z measurements at higher redshifts). This query is applied to the full catalogs (and not restricted to the ACT footprint), maintaining the constraint $M_{500} > 10^{14} M_{\odot}$. Besides, the search for matches is conducted in four disjoint redshift intervals, namely $[0.00, 0.35]$, $[0.35, 0.45]$, $[0.45, 0.55]$, and $[0.55, 0.80]$; the different interval sizes take into account the nonuniform redshift distributions of our cluster catalogs, allowing us to yield a comparable number of matches in each bin. The reason why we perform this analysis in different redshift bins is to allow for a possible z evolution in the agreement between the mass estimates from the different catalogs. The number of chosen redshift bins is rather arbitrary; in our case, four bins are enough to show any redshift trends, while retaining a number of matches per bin that is large enough for the subsequent analysis.

The results of the query for the cluster matches are shown in the left panels of Figures 3, 4, and 5 for the KiDS–WHL, KiDS–DESI, and WHL–DESI combinations, respectively. Each plot refers to one redshift interval, showing the comparison between the masses of the matched clusters, as obtained from the corresponding catalogs, together with the bisector $y = x$, which represents the ideal case of equality. In order to avoid excessive clutter in these plots, the mean error bars that are associated with the mass estimates are shown in separate boxes in the top left corners. We typically find around 100 cluster matches per redshift bin when considering the KiDS catalog, and we typically find more than 7000 matches for the combination of the larger WHL and DESI catalogs. In all plots, the masses are quoted in logarithmic units of $10^{14} M_{\odot}$,

which is a convenient choice, as it sets our low-mass threshold at the origin.

As expected, the intrinsic scatters of the scaling relations that are adopted to estimate each cluster mass, together with the uncertainties in the measurements of the associated mass proxies, determine the visible scatter of the points around the bisector. However, if the distribution of the points also shows any clear trends deviating from the bisector, the mass estimates that we adopt could be systematically biased. This effect is better visualized by splitting the points into different mass bins and only considering the associated mean masses that are computed for each catalog. In principle, the bins could be defined along each of the two coordinate axes, by choosing the corresponding catalog as a reference. In this case, however, the mass estimates from all the catalogs have significant error bars, meaning that this strategy for splitting the points is unreliable. In order not to make a preferential choice of any one catalog, we instead group the points in bins of equal separation from the line $y = -x$; or, in other words, we bin the points along the bisector, with the boundaries for each bin being the lines $y = -x + \Delta$ (with $\Delta \simeq 0.2$). In Figures 3 to 5, the mean masses of the points in each bin are shown as the red squares, while their standard deviations are quantified by the associated error bars.

In general, considering the mass uncertainties that are shown in the top left corners of the plots, the individual matches are compatible with the bisector within 1σ ; the mean points, however, in some cases reveal a trend or an offset that deviates from the bisector. It is then meaningful to correct for this effect by following the procedure that is adopted in Wen & Han (2015), where the same issue was encountered when building a calibration cluster sample by merging preexisting independent catalogs. We choose a reference catalog for the mass definition

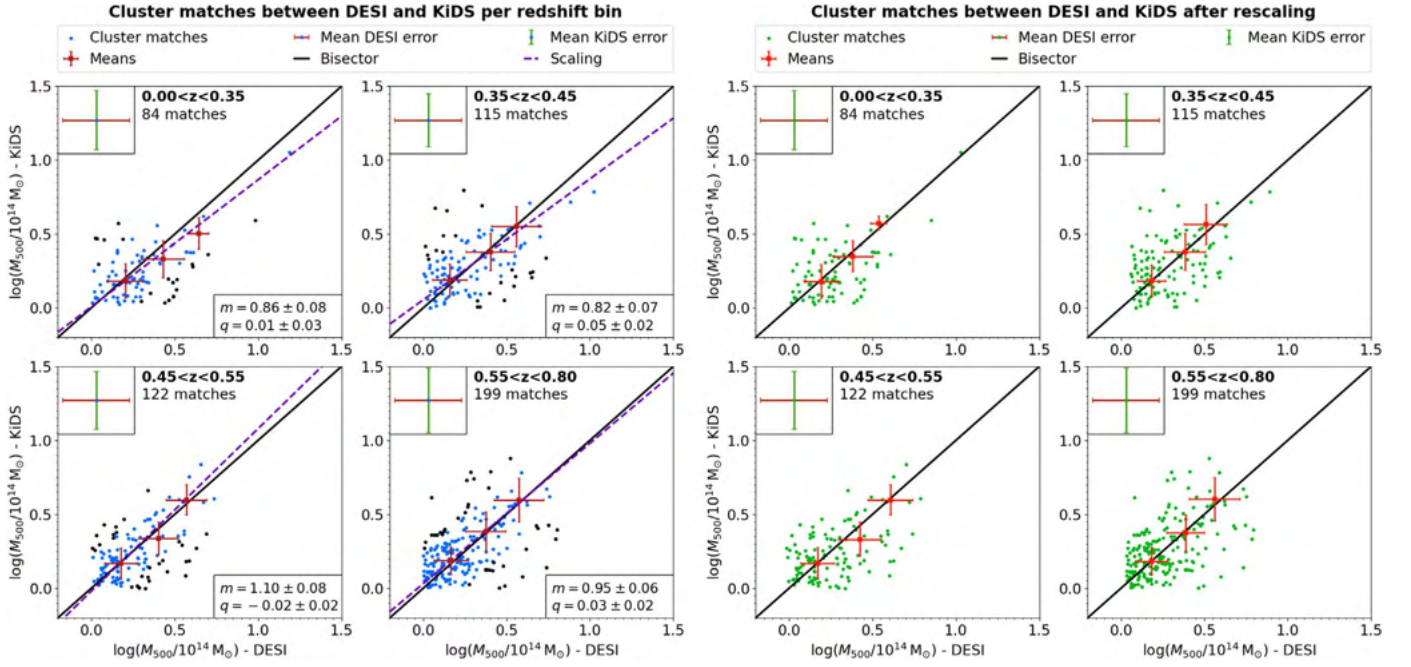


Figure 4. The same as Figure 3, but for the comparison between KiDS and DESI.

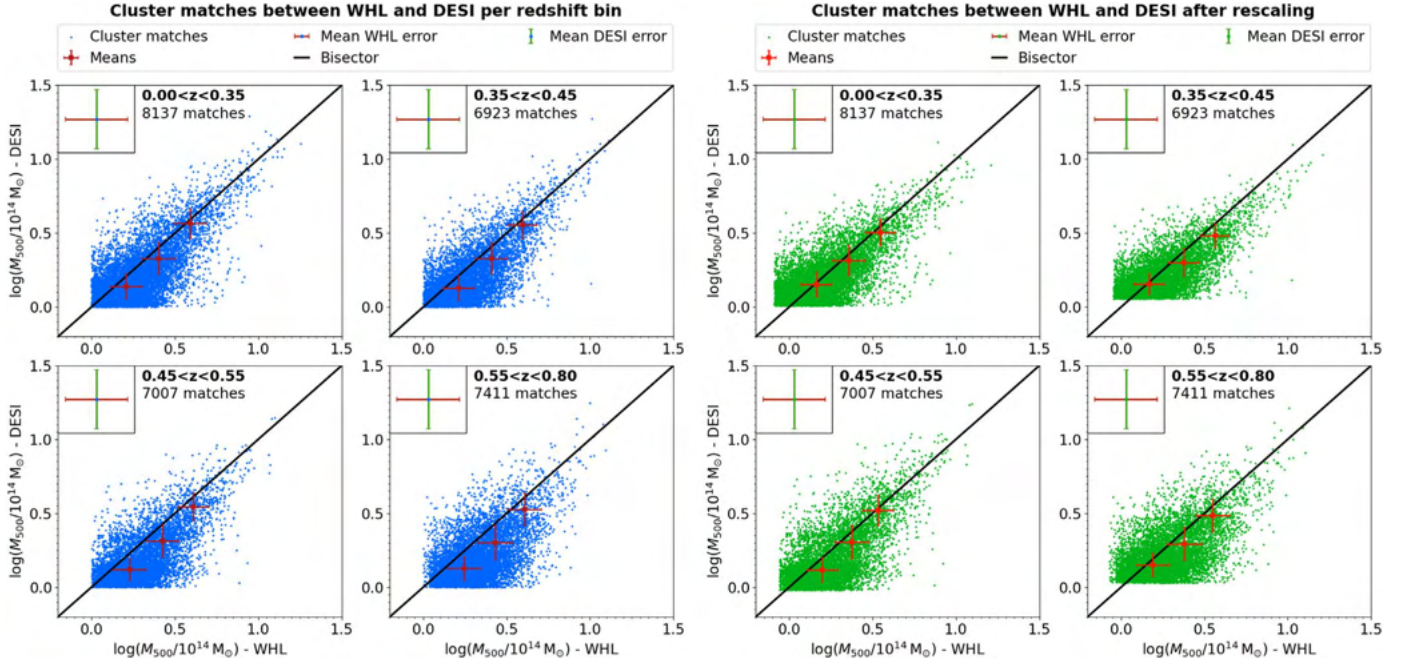


Figure 5. Similar to Figures 3 and 4, but for the comparison between DESI and WHL. In this case, no direct linear regression was employed to scale the WHL masses to match the DESI values, or vice versa; hence, the left panels do not include any fitting results. The right panels show the comparison between DESI and WHL, after the masses of both have been independently scaled to match the mass values from KiDS. Even in this case, the scaling yields a better agreement between the masses of the matched clusters from the two catalogs.

and rescale the masses of the other two catalogs to match the values from the reference one. The masses for the KiDS clusters are obtained via a richness–mass scaling relation that is calibrated on WL measurements, which directly probe the cluster masses, without any assumption of their physical states; hence, they can be considered more reliable than the masses quoted in WHL, which rely on the tSZ and X-ray masses that are defined in the calibration sample, or those quoted in DESI, which rely on abundance matching between the halo luminosity

and mass function. We shall therefore take KiDS as the reference catalog, and scale the masses from the other catalogs accordingly. For each redshift bin, the scaling has the form

$$\log_{10} \tilde{M}_{\text{KiDS}} = m_{X,i} \log_{10} \tilde{M}_X + q_{X,i}, \quad (4)$$

where $\tilde{M} \equiv M/(10^{14} M_\odot)$, X is either WHL or DESI, i selects the redshift bin, and the parameters m and q are obtained via linear regression on the masses of the associated matches.

In this context, the results from the linear regression can easily be biased by outliers. The latter could result from spurious matches or from the combinations of the intrinsic scatters in the scaling relations that are adopted to derive the cluster masses in the two catalogs (combined with the uncertainties in the measurements of the mass proxies themselves). In order for our fits not to be biased by these outliers, we identify and remove them according to the following procedure. In each of the mass bins that are bounded by the $y = -x + \Delta$ edge lines, we compute the orthogonal distance d of each point to the bisector and evaluate the associated standard deviation σ_d ; for each bin, we then discard all points for which $d > 2\sigma_d$ from the linear regression analysis. These outliers are shown in black in the left panels of Figures 3, 4, and 5. For the remaining points, due to the large error bars on both axes, an ordinary least squares fit would not be suitable; we instead adopt an orthogonal distance regression method, using the `SciPy` `ODR` package.²⁵ The resulting linear scalings are plotted as the dashed purple lines in Figures 3 and 4, where the boxes in the bottom right corners report the best-fit parameters. We notice that in all cases, the intercept satisfies $|q| < 0.1$; this result already suggests a broad consistency between the mass estimates from the different catalogs, as in the ideal case of $m = 1$, the intercept quantifies the mean offset between the two mass definitions. In the case of the KiDS–WHL comparison, the slope is always compatible with 1, while we find larger deviations for the KiDS–DESI case. However, we stress that the mean shift in mass that results from applying the scaling to the cluster samples that we use in the subsequent analysis (not only the subsamples of matched clusters) is equal to 0.06 dex for WHL and 0.02 dex for DESI, with maximum shifts of 0.09 dex and 0.16 dex, respectively. Hence, our mass correction is always below the initial mass uncertainty for individual clusters, and on average much smaller.

We can now use Equation (4) with the associated best-fit parameters to rescale the masses of WHL and DESI in each redshift bin. As DESI is the only catalog that extends at $z > 0.8$, its highest-redshift clusters have no matches with KiDS; hence, these cluster masses are not rescaled. The right panels of Figures 3 to 5 show once more the comparisons of the masses for the cluster matches, but this time after the mass rescaling has been applied; again, we overplot the bisector and mean masses with standard deviations for the $y = -x + \Delta$ bins. As already mentioned, our mass correction is small overall, so these plots resemble the ones shown in the left panels. Still, it is possible to appreciate how the agreements between the mean mass points and the bisector have marginally improved. It is interesting to consider the comparison between WHL and DESI in Figure 5; we notice that, in this case, no fitting function is overplotted in the left panel, as we did not consider the direct rescaling of the WHL masses to match the DESI values, or vice versa. Instead, both catalogs are independently rescaled to match the KiDS mass values of their associated matches. The comparison between the rescaled WHL and DESI masses is shown in the right panel of Figure 5. Again, the mean points over the $y = -x + \Delta$ bins show better agreement with the bisector, thus corroborating the consistency of our approach for mass recalibration.

In Appendix B, we quantify the impact of this mass rescaling on the final results of our study. We repeat the stacking analysis and parameter estimation on a different version of our cluster

Table 2

Summary of the Contributions from the KiDS, WHL, and DESI Catalogs to the Final Cluster Sample Employed in This Analysis

Catalog	N	N_{BN}	N_{D56}	$(z_{\text{min}}, z_{\text{max}})$
KiDS	806	806	0	[0.08, 0.74]
WHL	11,893	8937	2956	[0.04, 0.78]
DESI	11,121	8735	2386	[0.02, 0.97]
Total	23,820	18,478	5342	[0.02, 0.97]

Note. For each catalog, we report the number N of clusters overlapping with the ACT footprint, the numbers N_{BN} and N_{D56} of clusters located in the BN and D56 patches, respectively, and their redshift spans. These values refer to the WHL and DESI samples that are obtained after mass recalibration (Section 3.4) and the removal of overlapping objects (Section 3.5).

sample, obtained by merging the three catalogs without any explicit mass rescaling. We show that the differences in the final results are indeed much smaller than the statistical uncertainties that we quote on our parameter estimates.

3.5. The Joint Cluster Catalog

The mass rescaling described in the previous section is applied to the WHL and DESI catalogs, also including clusters with masses lower than $10^{14} M_{\odot}$; the cut $M_{500} > 10^{14} M_{\odot}$ is then subsequently applied to the mass-rescaled catalogs. This allows clusters with initial masses below our threshold to be included in the chosen sample, if the rescaling increases their M_{500} above $10^{14} M_{\odot}$. All catalogs are then queried to match the footprint of the two ACT patches, resulting in 806, 15,330, and 14,477 clusters in KiDS, WHL, and DESI, respectively. We then remove the cluster repetitions; the latter are identified by adopting the same positional matching criteria detailed in Section 3.4. From WHL and DESI, we remove all the clusters that match the KiDS positions, maintaining the corresponding entries in the KiDS catalog; as the latter have substantially lower statistics compared to WHL and DESI, this choice ensures that no KiDS cluster is discarded. For each remaining repetition between WHL and DESI, we maintain an entry from one of these catalogs, based on a random choice with equal probability. Overall, we remove 3437 clusters from WHL and 3356 clusters from DESI.

These cleared catalogs are then merged together to obtain the final sample that we employ for our study, which contains 23,820 clusters in total. The sample spans the mass range $M_{500} \in [10^{14.0}, 10^{15.1}] M_{\odot}$ and the redshift range $z \in [0.02, 0.97]$; a summary of the numbers of clusters for the different source catalogs and ACT patches is reported in Table 2. In the end, WHL and DESI contribute a comparable number of clusters to each ACT patch. The mass and redshift distributions of the final cluster sample, combining objects from both ACT patches, are shown in Figure 6.

4. The Mean Cluster Compton Profiles

In this section, we describe the methodology that we adopt to measure the mean angular y -profiles from our cluster samples, and discuss the results.

4.1. Cluster Binning

The main goal of this study is to explore the dependence of the cluster pressure profile on mass and redshift. To this end, we define a set of three bins in $\log_{10}(M_{500})$, bounded by the values [14.0, 14.3, 14.6, 15.1], and three bins in z , bounded by the values [0.00,

²⁵ <https://docs.scipy.org/doc/scipy/reference/odr.html>

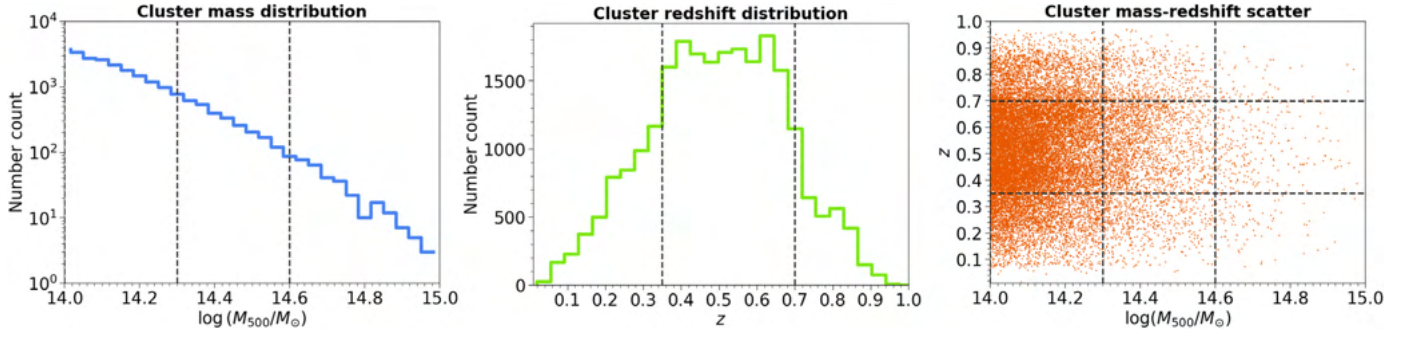


Figure 6. Statistics of the full cluster sample employed in this study. The left and middle panels show the cluster number distributions in mass and redshift, respectively, while the right panel shows the joint distribution of the two variables. In each panel, the dashed lines mark the boundaries of the chosen mass and/or redshift bins, as detailed in Section 4.1.

Table 3

Significances per Bin χ_b^2 of the Mean y -profile Measurements for All the Considered M - z Bins, for Both Planck and ACT, Computed as in Equation (10)

	M_{500}	$[10^{14.0}, 10^{14.3}] M_{\odot}$	$[10^{14.3}, 10^{14.6}] M_{\odot}$	$[10^{14.6}, 10^{15.1}] M_{\odot}$	All M_{500}
z					
N_{cl}	[0.00, 0.35]	3652	673	96	4421
χ_b^2 (Planck)		62.4	107.0	91.4	157.7
χ_b^2 (ACT)		5.8	6.2	5.1	7.8
N_{cl}	[0.35, 0.70]	13,518	2125	243	15,886
χ_b^2 (Planck)		33.0	76.3	125.5	82.0
χ_b^2 (ACT)		7.6	9.4	6.0	10.0
N_{cl}	[0.70, 1.00]	2840	620	53	3513
χ_b^2 (Planck)		13.3	19.0	23.5	30.1
χ_b^2 (ACT)		4.1	4.3	3.0	6.4
N_{cl}	All z	20,010	3418	392	23,820
χ_b^2 (Planck)		94.2	160.5	179.6	229.0
χ_b^2 (ACT)		9.7	11.4	7.7	12.4

Note. The table also reports the number of clusters stacked in each case. For clarity, the number of clusters in each bin is reported in bold.

0.35, 0.70, 1.00]. We then split our cluster catalog into a set of nine subsamples, with each belonging to a combination of a mass bin and a redshift bin. The last panel in Figure 6 is a scatter plot, showing the distribution of the clusters in the $(\log_{10}(M_{500}), z)$ plane; this plot shows that there is no strong correlation between the two variables, most likely as a result of the catalogs being nearly complete above the chosen mass cut, so the choice of redshift bin is independent of the choice of mass bin and it is meaningful to adopt the same set of M_{500} boundaries across the whole z range. We also consider the marginalized samples obtained by joining all the redshift values for each mass bin, and vice versa. Finally, we include the full cluster sample as the marginalized case over both variables. We obtain in this way a total of 16 different cluster samples (the full sample, nine disjoint subsamples, and six marginalized cases), which we employ separately to measure the mean Compton parameter profile. Hereafter, we shall refer to them as M - z bins.

Our choice for the number of bins in M_{500} and z ensures that we have enough statistics for the stacking analysis in each M - z bin, while at the same time allowing us to investigate the possible dependencies in mass and redshift. We follow the same choice as adopted by G19 and consider three bins in redshift, which are almost equally spaced over the range

spanned by the cluster sample. We also adopt three bins for the masses; however, given the steep decrease in the numbers of objects for increasing masses, the top M_{500} bin is in this case chosen to be wider, in order to retain sufficient statistics for the stacking analysis described in Section 4.2. Clearly, in the end, we will have a different number of clusters in each M - z bin; this, however, is not an issue for our analysis. The formalism that we adopt to model our measurements, which is described in Section 5.3, naturally accounts for the number of objects and the mass span for each case. The final numbers of clusters included in each of the M - z bins are reported in Table 3.

4.2. Cluster Stacks and Angular Profiles

For each of our 16 cluster samples, we obtain an independent stacked map. Let N_{cl} be the number of clusters in one M - z bin; for the generic i th cluster, we trim a local submap, centered on its nominal coordinates, with size $30' \times 30'$ in the case of Planck and $15' \times 15'$ in the case of ACT.²⁶ We label such a map S_i , which carries information about the y -signal around the

²⁶ These different values are a result of the different beam sizes for the two maps, and they are chosen to enable a reconstruction of the whole cluster signal and part of the neighboring background—see Figures 7 and 8.

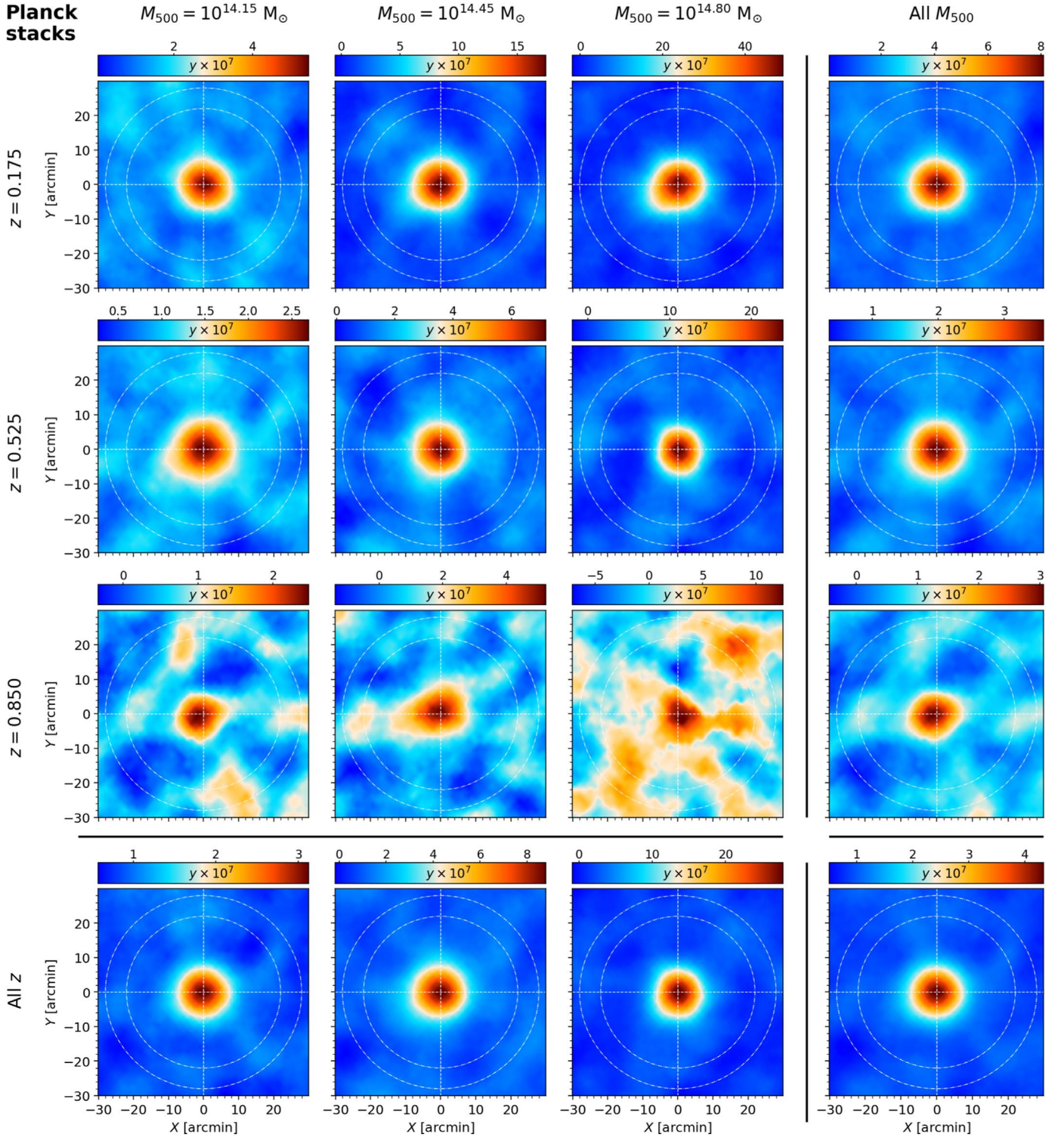
Planck stacks


Figure 7. Stacking results for the Planck y -map. Each row (column) represents a selected redshift (mass) bin, with the last one showing the marginalized case over the full redshift (mass) range. Notice that the color scales reported above each panel are not the same and are chosen to saturate each stack. In each panel, the nominal center of the stack is marked by the dashed white lines, while the dotted–dashed lines mark the inner and outer boundaries of the annulus employed to estimate the mean background level.

cluster; we also obtain an equivalent weight map W_i , which is extracted in the same way from the corresponding survey mask. The y -stack map S for the considered sample is then obtained as

$$S = \frac{1}{W} \sum_{i=1}^{N_{cl}} S_i W_i, \quad (5)$$

where the total weight is given by

$$W = \sum_{i=1}^{N_{cl}} W_i. \quad (6)$$

The resulting 16 stacks for each M - z bin are shown in Figure 7 for the Planck map and Figure 8 for the ACT map. For each

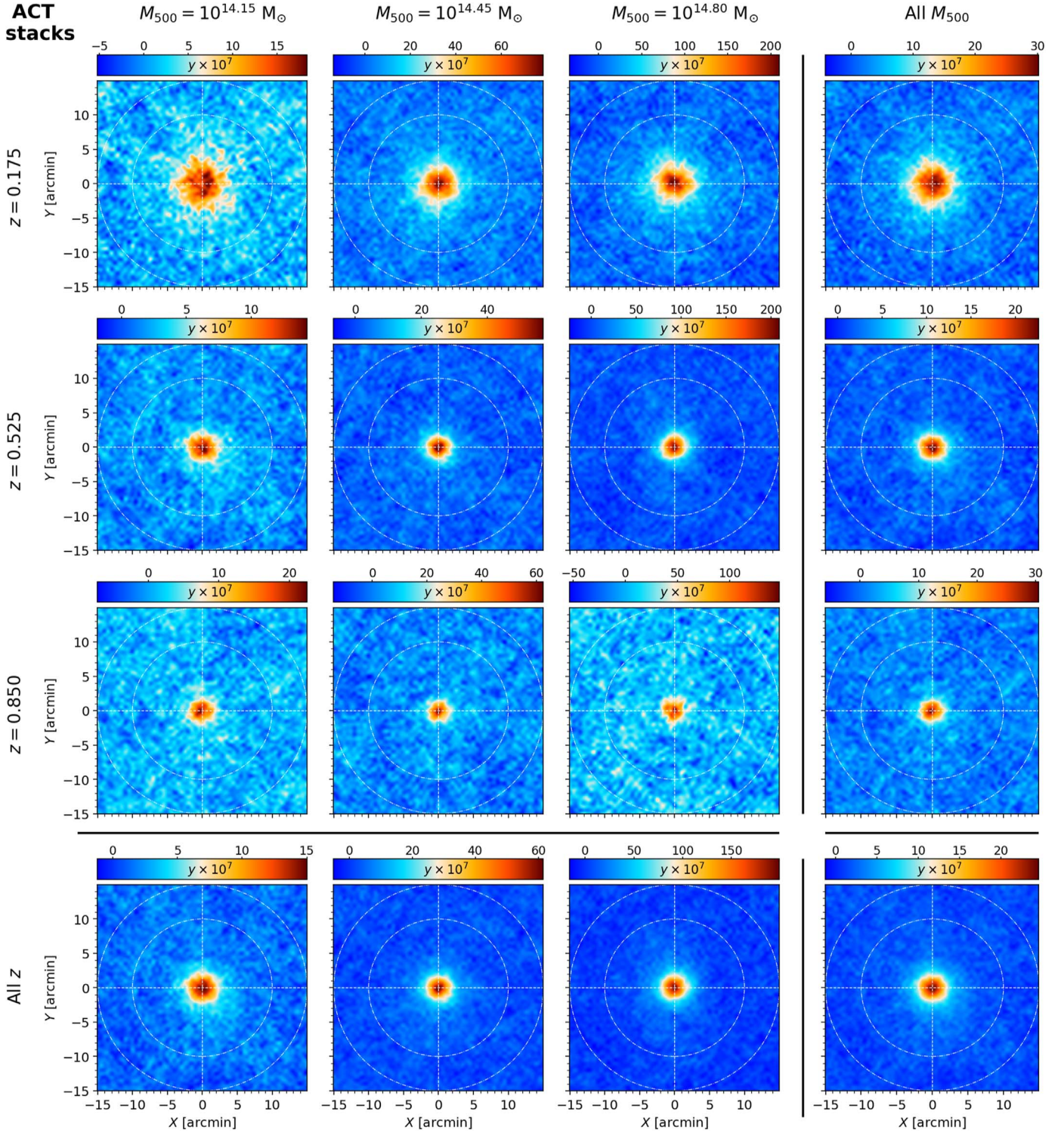


Figure 8. The same as Figure 7, but for the ACT y-map.

stack, the axes show the angular separation from the center, which is also marked with a pair of white dashed lines.

From each of these stacks, we can derive the associated Compton parameter profile, $y(\theta)$, as a function of the angular separation θ from the cluster center. The profile is built by splitting the pixels over a set of N_b bins in the angular separation from the map center, then taking the mean value in each bin. As we are interested in the contrast of the local cluster

signal, we first quantify a mean background value to be subtracted from each map.²⁷ The latter is estimated by repeating, for each $M-z$ bin, the Compton y-stack, using 500 different replicas of the associated cluster sample, where in each case the cluster coordinates are randomly shuffled within the allowed ACT footprint. This results in 500 radial profiles

²⁷ The stacks plotted in Figures 7 and 8 are not background-subtracted.

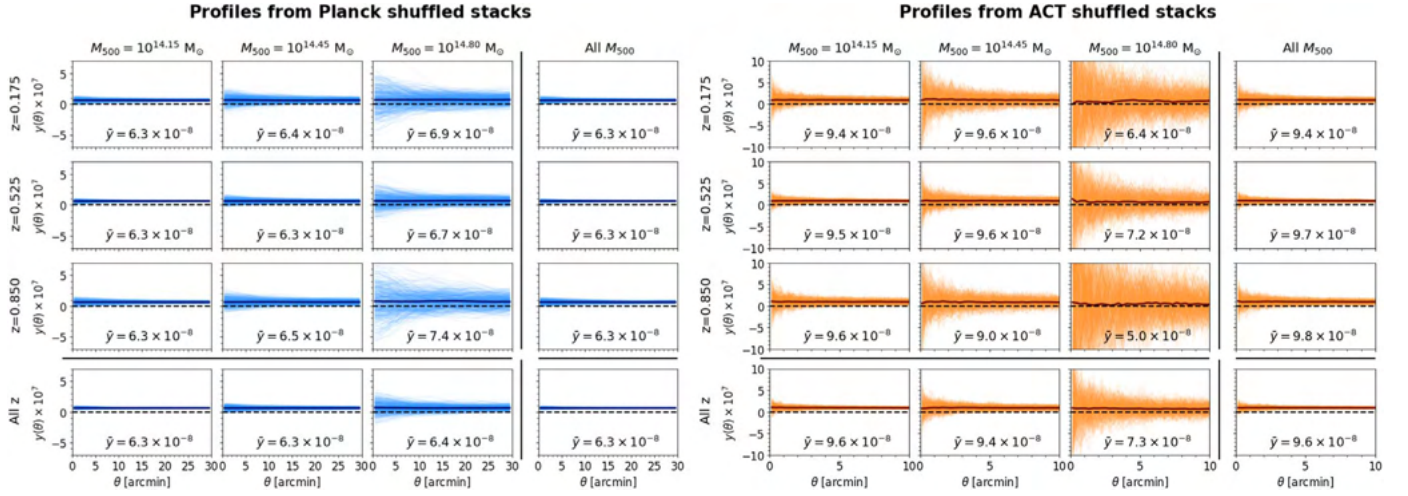


Figure 9. Estimation of the mean background values for each M - z bin, for both the Planck (left) and ACT (right) maps. For each panel, we show the profiles obtained by stacking 500 replicas of the corresponding cluster sample, each obtained by randomly shuffling the cluster positions. The thick solid line shows the average profile; the mean amplitude \bar{y} of the latter over the considered angular range is explicitly quoted in each panel. The zero level is marked by the dashed line.

per M - z bin; the resulting mean is used to evaluate the background contribution as a function of θ , and is subtracted from the corresponding M - z stack obtained using the real cluster sample. The results are shown in Figure 9 for both ACT and Planck. We notice that in all cases, the mean profile does not show any strong dependence on the angular separation from the center; we then quote in each panel the mean value \bar{y} of the average profile over the considered θ range (i.e., up to 30' for Planck and 10' for ACT). We stress that the clusters from the different M - z bins actually span the same area, which is set by the ACT patch boundaries. Hence, we would expect to obtain the same estimate for the mean background level from the different cluster samples. Figure 9 shows that this is in general verified, with the exception of the top-mass bin, which displays larger deviations. This is due to the much lower number of clusters in this mass range, which produces a considerably larger spread of the individual shuffled profiles around the mean (the effect is more relevant for ACT). However, for all these M - z bins, the stack amplitudes from Figures 7 and 8 are high enough that this zero-level correction is negligible ($\lesssim 1\%$ at the profile peak). For the lower-mass bins, instead, the estimates of the mean background level converge to the values of $\bar{y} = 6.3 \times 10^{-8}$ for Planck and $\bar{y} = 9.6 \times 10^{-8}$ for ACT.

Even after the removal of the background contribution, as described above, the y -profiles do not always reach a null amplitude for large θ values. We then subtract from each profile an additional zero-level contribution, measured as the average of the y -values from the pixels bounded by a circular annulus outside the cluster outskirts. The inner and outer annulus radii are [22, 28] arcminutes for Planck and [10, 15] arcminutes for ACT, chosen in such a way as to exclude any cluster signal contribution (see again Figures 7 and 8, for reference). Notice that this operation will be also applied to our theoretical predictions for the cluster profile—see Equation (31). The final background-subtracted profiles are shown in Figure 10, for both Planck and ACT (the left and right panels, respectively). These figures focus on the comparisons between the profiles for the different redshift samples, for each cluster mass bin.

To complete the statistical characterization of our measurements, we compute the covariance matrices associated with the profiles. Again, for each M - z bin, we perform stacks of

$N_{\text{rand}} = 500$ replicas of the associated cluster sample, obtained via bootstrap resampling (each randomized catalog is obtained by randomly selecting clusters from the original sample, up to the same number N_{cl} , with the possibility of repetition). The covariance between the two angular separations θ_i and θ_j can then be computed as

$$C(\theta_i, \theta_j) = \frac{1}{N_{\text{rand}}} \sum_{k=1}^{N_{\text{rand}}} [y_k(\theta_i) - \bar{y}(\theta_i)][y_k(\theta_j) - \bar{y}(\theta_j)], \quad (7)$$

where y_k denotes the k th random profile and \bar{y} is the average profile of the random realizations:

$$\bar{y}(\theta_i) = \frac{1}{N_{\text{rand}}} \sum_{k=1}^{N_{\text{rand}}} y_k(\theta_i). \quad (8)$$

By construction, the diagonal of each covariance matrix quantifies the profile variance at the corresponding angular separation, $\sigma^2(\theta_i) = C(\theta_i, \theta_i)$; these $\sigma(\theta_i)$ values are the effective uncertainties in our profile measurements, and are shown as the shaded regions in Figure 10. In Figure 11, we show, for both Planck and ACT, the 16 associated correlation matrices, which are obtained from the covariance matrices as:

$$\text{Corr}(\theta_i, \theta_j) = \frac{C(\theta_i, \theta_j)}{\sigma(\theta_i)\sigma(\theta_j)}. \quad (9)$$

The covariance matrices also allow us to compute the significance of the measured y -profile for each M - z bin, defined as the chi-squared value:

$$\chi^2 = \sum_{i=1}^{N_b} \sum_{j=1}^{N_b} y(\theta_i) I(\theta_i, \theta_j) y(\theta_j), \quad (10)$$

where I is the inverse of the covariance matrix, corrected by an overall scaling factor, to yield an unbiased estimator (Hartlap et al. 2007):

$$I(\theta_i, \theta_j) = \frac{N_{\text{rand}} - N_b - 2}{N_{\text{rand}} - 1} C^{-1}(\theta_i, \theta_j). \quad (11)$$

The significance for all the stacks is reported in Table 3, together with the number of clusters in each sample. As the

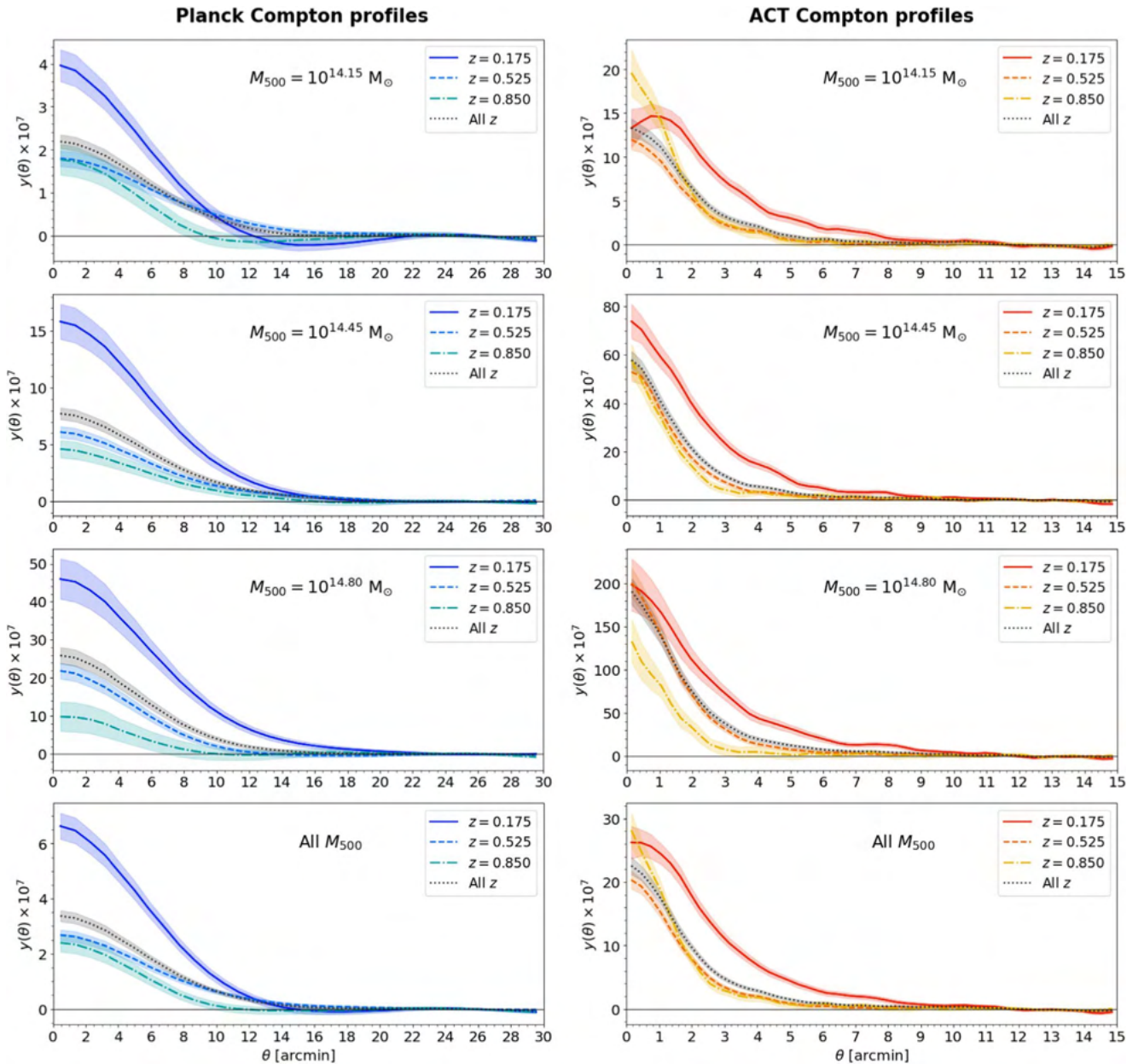


Figure 10. Radial profiles obtained from the stacks that are shown in Figures 7 and 8. The left column shows the results for Planck, while the right column shows the results for ACT. Each row corresponds to a chosen M_{500} bin, with the bottom row showing the marginalized case over all masses. Each panel shows the results from the three redshift bins and for the marginalized case over all redshifts; the shaded area around each profile quantifies the associated 1σ uncertainty.

quantity from Equation (10) depends on the number of bins considered, we quote the significance per bin, defined as $\chi_b^2 = \chi^2/N_b$, where N_b is the number of angular bins until the inner radius of the annulus employed to estimate the background value (33 for ACT and 24 for Planck). Since we are not using the χ^2 estimate to fit for a model, the number of degrees of freedom is equal to the number of bins. Hence, our χ_b^2 measurement is in fact a reduced- χ^2 measurement for the null model $y(\theta) = 0$, which can be used to evaluate the significance of the detection.

4.3. Discussion of Profile Measurements

Figures 7 and 8 show that the cluster signal is clearly detected in all cases; in order to better show its contrast with

respect to the background, the color scale for each stack is chosen to saturate the signal. The main difference between the Planck and ACT results is the resolution of the reconstructed signal, as expected. The much larger Planck beam implies not only that the cluster signal is artificially broadened to larger angular separations from the stack center, but also that most of the features on scales below a few arcminutes are smoothed out. The ACT stacks, instead, allow for a more accurate reconstruction of the same signal, at smaller scales. A larger beam also implies a more severe dilution of the cluster signal, as becomes evident by comparing the amplitudes of any stacks between the two y -maps.

As expected, for each survey, we see that the significances of the stacks tend to be lower for decreasing mass and increasing redshift. This is much clearer for the ACT stacks, which are less affected by the smoothing effect of the beam convolution.

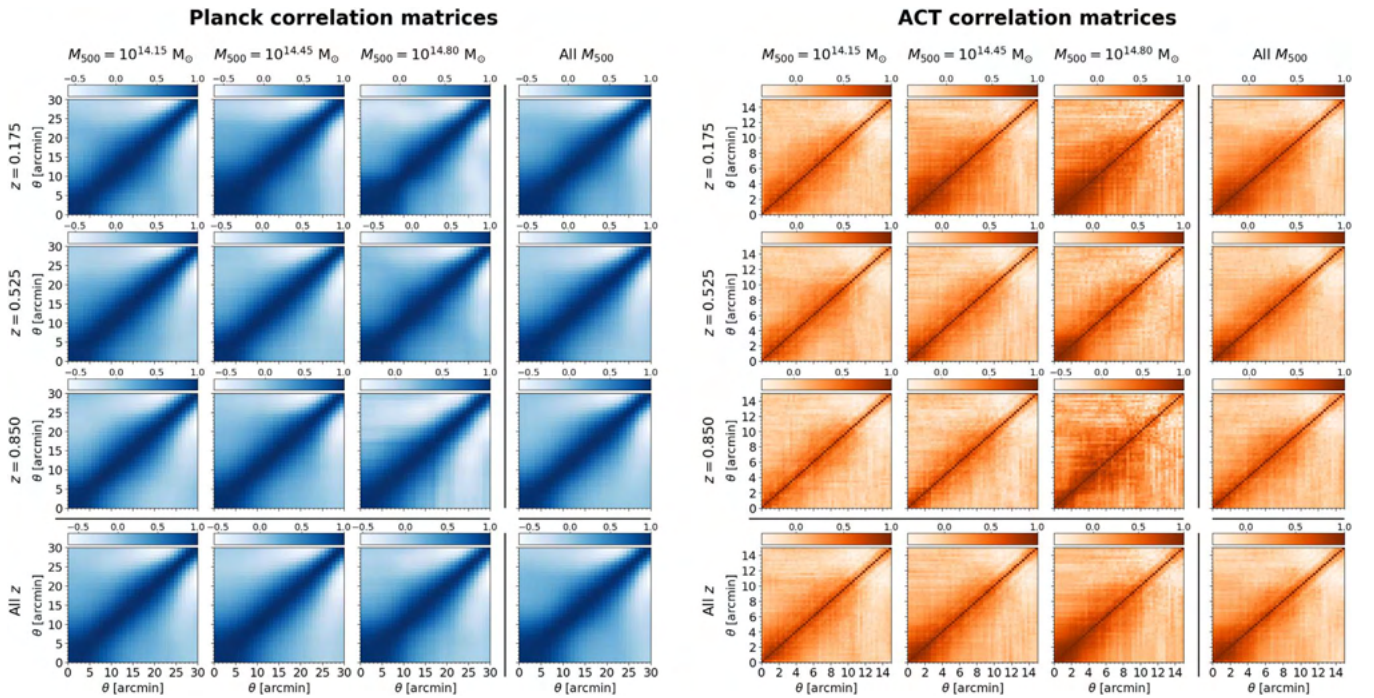


Figure 11. Correlation matrices computed from the randomized stacks, as described in Section 4.2. Results are shown for Planck on the left and ACT on the right, using the same M_{500} , z binning scheme as adopted in Figures 7 and 8.

The reduction in mass determines the highest variations of the signal amplitude and in general yields more irregular stacks. The much higher statistics that are available for the lowest-mass bin (the first panel of Figure 6) ensure that the cluster signal is still detected, despite the significant drop in the S/N that is expected for individual objects in this M_{500} range. The increase in redshift also produces a decrease in the signal amplitude (although to a lesser extent compared to the mass change), with the highest-redshift bin showing stronger background fluctuations. The small ACT beam also allows us to appreciate the shrinking of the cluster signal for increasing redshift, as the angular diameter distance monotonically increases with z in the redshift range that we explore. The decrease in the profile amplitude with z could be a result of the higher-redshift clusters being in earlier stages of evolution, and, as such, possibly not yet being fully virialized, which would lower the associated SZ signal (we remind the reader that our cluster sample is selected on the basis of optical observations, which cannot probe the ICM directly). Besides, higher- z clusters subtend smaller angular scales and are therefore more severely affected by the beam smoothing effect; this could account for the higher z dependence of the profile amplitudes observed in the Planck stacks compared to the ACT stacks. The marginalized cases over M_{500} typically show features in between those of the two lowest-mass bins, as those encompass the vast majority of the clusters in our samples. The marginalized cases over z are instead quite similar to the mid-redshift bin, as the cluster numbers in the different z bins are comparable. Finally, the marginalized case over both M_{500} and z shows the highest S/N and the most regular, rounded cluster emission, as is expected from the exploitation of the full cluster statistics.

Most of these considerations can also be inferred from the angular profiles in Figure 10. Notice that, because each panel compares profiles from different redshift bins, they do not

include the associated instrumental beam profile, to avoid excessive clutter. A direct comparison between each measured y -profile and the beam profile (scaled to the measured peak amplitude) will be shown later, in Figures 13 and 14. Those figures prove that the measured profiles extend to higher angular separations than the instrumental beam, i.e., the profiles are resolved in all cases; it is then meaningful to employ them to fit for the underlying pressure profile parameters (Section 6), even for the case of Planck. Going back to Figure 10, we see that the profiles for Planck always show a regular trend, also thanks to the smoothing effect from the large instrumental beam: for a chosen M_{500} bin, the profiles have similar shapes, with the amplitude steadily decreasing for increasing z , and with the marginalized case over all redshifts being generally close to the mid- z sample. The higher resolution of ACT instead allows more irregularities to be revealed in the profiles. The case of the bin with the lowest mass and redshift shows a decrease in the profile amplitude toward the stack center; this results from the peak of the stacked signal being located off-center, as is clear to see from the corresponding stack panel in Figure 8. This could be due to possible contamination from the neighboring high-mass clusters, or to a mismatch between the sample cluster nominal and real central positions; the latter possibility will be taken into account in our modeling in Section 5.4. We also notice that for the top-mass bin, the top- and mid-redshift bins have comparable peak amplitudes; once again, this is probably due to a miscentering effect, which artificially dilutes the signal amplitude and becomes more relevant for lower redshifts. We conclude this section by commenting on the correlation matrices plotted in Figure 11. The angular y -profile is expected to introduce correlations between neighboring θ bins. This is indeed reflected in the plots, especially for the lowest angular separations. Once again, the situation is remarkably different depending on the survey considered, with the correlation extending up to a scale of

$\sim 1' - 2'$ in the case of ACT and up to $\sim 10'$ in the case of Planck, as expected from the different FWHMs. For each survey, the correlation matrices do not show appreciable dependencies on the chosen mass and redshift bins. The diagonal values of the covariance matrices are the squares of the uncertainties overplotted to the radial profiles, as shown by the shaded areas in Figure 10. We see that the number of clusters stacked in each case partially affects the magnitude of the uncertainties, with the marginalized cases generally showing smaller error bars. This is also reflected in the significance values that are quoted in Table 3. As expected, the detection significance increases for high masses and low redshifts, for both Planck and ACT, but it is also partially affected by the number of clusters in the associated sample. We can quote the square root of the χ_b^2 values as the detection significance per bin in σ units. The significance per bin is typically above $\sim 3.6\sigma$ for Planck and $\sim 1.7\sigma$ for ACT, and reaches the top values of 15.1σ and 3.5σ , respectively, for the stack of the full cluster sample. The higher significances that are associated with the Planck measurements are a result of the lower uncertainties in the reconstructed profiles, which, in turn, are due to the smoothing effect of the larger beam.

5. Theoretical Modeling

The following details the formalism that we adopt to theoretically predict the Compton profiles that are presented in the previous section.

5.1. The Pressure Profile for Individual Clusters

The electron pressure profile P_e for a galaxy cluster of mass M_{500} at redshift z can be written as

$$P_e(r; M_{500}, z) = P_{500}(M_{500}, z) f(M_{500}, z) \times \mathbb{P}(x = r/\tilde{R}_{500}). \quad (12)$$

Here, $\mathbb{P}(x)$ is the UPP that has already been defined in Equation (3) and P_{500} is the characteristic cluster pressure that is expected in the self-similar model:

$$\frac{P_{500}(M_{500}, z)}{\text{keV cm}^{-3}} = 1.65 \times 10^{-3} E(z)^{8/3} \times \left[\frac{(1 - b_h) M_{500}}{3 \times 10^{14} h_{70}^{-1} M_\odot} \right]^{2/3} h_{70}^2, \quad (13)$$

where $E(z) \equiv H(z)/H_0 = \sqrt{\Omega_m(1+z)^3 + \Omega_\Lambda}$, with $\Omega_\Lambda = 1 - \Omega_m$ for flatness, $h_{70} = h/0.7$, and b_h being the hydrostatic mass bias. A similar expression, but without the inclusion of the $(1 - b_h)$ factor, was also employed in Arnaud et al. (2010); in that work, cluster masses were derived from scaling relations based on the quantity Y_X , defined as the product between the gas mass within R_{500} and the spectral temperature T_X (see also Nagai et al. 2007). Such mass estimates rely on the assumption of local hydrostatic equilibrium in the ICM, and can therefore be biased with respect to the true cluster masses. As we employ mass definitions based on lensing observations in this paper, which probe the true cluster mass content, we account for this bias by explicitly introducing the $(1 - b_h)$ factor to scale our M_{500} values in Equation (13). The bias b_h will be left free in our analysis and estimated together with the other UPP parameters. We remind the reader that the introduction of the hydrostatic bias also affects the

definition of the scale radius in the computation of the pressure profile, i.e., $x \equiv r/\tilde{R}_{500}$, with $\tilde{R}_{500} = R_{500}(1 - b_h)^{1/3}$.

We notice that Equation (12) differs from the expression in Equation (3), which was the initial ansatz proposed by Nagai et al. (2007), by an additional factor $f(M_{500}, z)$. The latter determines a break in the self-similarity and was introduced by Arnaud et al. (2010), to accommodate a residual mass dependence found in the scaled X-ray pressure profiles. When parameterized around the same pivot mass $M_{500} = 3 \times 10^{14} h_{70}^{-1} M_\odot$, it reads

$$f(x; M_{500}, z) = \left[\frac{(1 - b_h) M_{500}}{3 \times 10^{14} h_{70}^{-1} M_\odot} \right]^{\alpha_p}, \quad (14)$$

with $\alpha_p = 0.12$ and where we again explicitly introduce the bias correction factor $(1 - b_h)$.

5.2. The Mean Compton Profile for a Population of Clusters

The profiles obtained from our stacks contain contributions from a large number of clusters with different mass and redshift values. Formally, such a merged profile can be evaluated as the two-point correlation between the Compton y -map and the cluster sample, which, in turn, can be obtained by inverse Fourier transform of the associated cross-correlation power spectrum C_ℓ^{yc} :

$$y(\theta) = \int d\ell \frac{\ell}{2\pi} J_0(\ell\theta) C_\ell^{yc} B_\ell, \quad (15)$$

with ℓ being the multipole and J_0 the zeroth-order Bessel function. In order to account for the instrumental smoothing of the reconstructed Compton map, the expression also includes the beam window function B_ℓ :

$$B_\ell = \exp \left[-\frac{1}{2} \ell(\ell + 1) \sigma_b^2 \right], \quad (16)$$

where $\sigma_b = \theta_{\text{FWHM}}/\sqrt{8 \ln 2}$. The cross-correlation power spectrum C_ℓ^{yc} can be computed using a halo model framework, which considers the contribution of both a one-halo and a two-halo term, as (Komatsu & Kitayama 1999)

$$C_\ell^{yc} = C_\ell^{yc,1} + C_\ell^{yc,2}. \quad (17)$$

The one-halo term $C_\ell^{yc,1}$ quantifies the integrated contribution of the individual clusters, and is computed as

$$C_\ell^{yc,1} = \frac{1}{\bar{n}_c} \int dz \frac{d^2V}{d\Omega dz}(z) \int dM \frac{dn}{dM}(M, z) \times S(M, z) \tilde{y}_\ell(M, z), \quad (18)$$

where the integrals are weighted by the comoving volume element $d^2V/d\Omega dz = c \chi^2/H(z)$ (χ is the comoving distance to redshift z) and the halo mass function dn/dM (e.g., Tinker et al. 2008). The selection function $S(M, z)$ depends on the particular cluster sample that we consider; it encodes any deviations from the theoretical mass function, due to observational selection effects and other constraints applied to our catalogs. The entire expression is normalized by the mean angular number density of the halos \bar{n}_c , given by (see also, e.g., Fang et al. 2012)

$$\bar{n}_c = \int dz \frac{d^2V}{d\Omega dz} \int dM \frac{dn}{dM}(M, z) S(M, z). \quad (19)$$

The quantity \tilde{y}_ℓ in Equation (18) is the Fourier transform of the Compton parameter profile, which can be computed as

$$\tilde{y}_\ell(M, z) = \frac{\sigma_T}{m_e c^2} \frac{4\pi \tilde{R}_{500}}{\ell_s^2} \times \int dx x^2 \frac{\sin(\ell x / \ell_s)}{\ell x / \ell_s} P_e(x; M, z), \quad (20)$$

where $\ell_s = d_A / R_{500}$ and d_A is the angular diameter distance; the expression contains the cluster electron pressure profile P_e , defined in Equation (12), and the radius \tilde{R}_{500} , corrected for hydrostatic bias.

The two-halo term $C_\ell^{\text{yc},2}$ quantifies the correlation between the different clusters, and is computed as

$$C_\ell^{\text{yc},2} = \frac{1}{\bar{n}_c} \int dz \frac{d^2 V}{d\Omega d\Omega z} W_\ell^y(z) P_m\left(k = \frac{\ell + 0.5}{\chi(z)}, z\right) \times \int dM \frac{dn}{dM}(M, z) S(M, z) b(M, z), \quad (21)$$

where $P_m(k, z)$ is the linear matter power spectrum, $b(M, z)$ is the linear halo bias, and

$$W_\ell^y(z) = \int dM \frac{dn}{dM}(M, z) b(M, z) \tilde{y}_\ell(M, z). \quad (22)$$

We compute the linear halo bias by adopting the parameterization from Tinker et al. (2010).

5.3. Application to Our Sample

In our case, the selection function $S(M, z)$ cannot simply be expressed as a combined cut in mass and redshift, depending on the chosen M - z bin. Due to the extended processing of the cluster catalogs prior to the stacking analysis, as described in Sections 3.4 and 3.5, the selection function cannot be modeled analytically. A solution proposed in G19 consists of splitting the mass and redshift ranges into a set of smaller N_M and N_z intervals,²⁸ respectively. We call \bar{M}_i and \bar{z}_j the mean values within the generic i th mass and j th redshift intervals. Within each interval, the integral evaluation can be reasonably approximated as the product of the interval width and the integrand function evaluated at the interval mean value. For the generic i th mass and j th redshift interval, the one-halo term then reads

$$C_\ell^{\text{yc},1}(\bar{M}_i, \bar{z}_j) = \tilde{y}_\ell(\bar{M}_i, \bar{z}_j), \quad (23)$$

i.e., it is simply equal to the Compton Fourier transform as evaluated at the mean redshift and mass. For the two-halo term, we have

$$C_\ell^{\text{yc},2}(\bar{M}_i, \bar{z}_j) = b(\bar{M}_i, \bar{z}_j) \times P_m\left(k = \frac{\ell + 0.5}{\chi(\bar{z}_j)}, \bar{z}_j\right) W_\ell^y(\bar{z}_j). \quad (24)$$

In this case, the quantity $W_\ell^y(\bar{z}_j)$ still needs to be evaluated via a full mass integral, as in Equation (22). In summary, when

²⁸ To avoid confusion, we continue to use the word ‘‘bin’’ to denote each of the redshift and mass choices that generate the 16 M - z cluster samples that we stack on the y -map, while the word ‘‘interval’’ designates the further splitting of each bin into smaller separations in mass and redshift.

working with intervals, Equations (23) and (24) replace Equations (18) and (21), respectively.

For both the one-halo and two-halo terms, the full quantity over the chosen cluster sample can be recovered as

$$C_\ell^{\text{yc},X} = \frac{1}{N_{\text{cl}}} \sum_i^{N_M} \sum_j^{N_z} n_{ij} C_\ell^{\text{yc},X}(\bar{M}_i, \bar{z}_j), \quad (25)$$

where X is either 1 or 2, or even the sum of both halo terms. The factor n_{ij} is the number of clusters with mass and redshift within the i th mass and j th redshift interval, such that the total number of clusters N_{cl} in the chosen M - z bin is recovered as

$$N_{\text{cl}} = \sum_{i=1}^{N_M} \sum_{j=1}^{N_z} n_{ij}. \quad (26)$$

The expression in Equation (25) ensures that all selections that are applied to build the considered cluster sample will also be accounted for in the theoretical modeling of the associated mean Compton profile.

We stress that a direct approach, based on computing the individual $y(\theta; M_{500}, z)$ profile for each stacked cluster and considering the resulting mean value, would not be adequate for our analysis. First, such an approach would not take into account the intercluster correlations and would only consider the contribution from the one-halo term; and second, the computation of $\sim 10^4$ profiles would be unpractical for the parameter estimation methodology described in Section 6. The use of Equations (23) to (25) allows us to solve both these issues. In our implementation, we adopt $N_M = 5$ and $N_z = 5$ when dealing with individual M - z cross bins, and $N_M = 15$ and $N_z = 15$ when dealing with mass- or redshift-marginalized cases, respectively. We checked that this choice yields deviations $< 1\%$ from the theoretical profile that is obtained by adopting the full formalism from Equations (18) and (21) (with the n_{ij} factors being computed by integrating the halo mass function over the chosen mass and redshift intervals), which is within the error bars of our measurements (Figure 10).

5.4. Miscentering and Zero Level

In our modeling, we consider possible offsets of the real cluster centers with respect to their quoted coordinates (Yan et al. 2020). For the stacking analysis, this would imply that the reconstructed profile is artificially diluted, meaning that we actually measure a mean ‘‘offset’’ profile $\bar{y}_{\text{off}}(\theta)$ instead of the true intrinsic profile $y(\theta)$. We follow the approach presented in Bellagamba et al. (2018) and Giocoli et al. (2021) by dividing the cluster population into a fraction f_{off} , which is affected by miscentering, and a fraction $1 - f_{\text{off}}$, whose true cluster positions coincide with the nominal ones. The observed resulting miscentered profile y_{msc} is then

$$y_{\text{msc}}(\theta) = f_{\text{off}} \bar{y}_{\text{off}}(\theta) + (1 - f_{\text{off}}) y(\theta). \quad (27)$$

The problem therefore reduces to the computation of the mean offset profile $\bar{y}_{\text{off}}(\theta)$. For a known angular offset θ_{off} , the miscentered profile $y_{\text{off}}(\theta | \theta_{\text{off}})$ can be computed starting from the centered profile $y(\theta)$, as (Yang et al. 2006)

$$y_{\text{off}}(\theta | \theta_{\text{off}}) = \frac{1}{2\pi} \times \int_0^\infty d\varphi y(\sqrt{(\theta^2 + \theta_{\text{off}}^2 + 2\theta\theta_{\text{off}}\cos\varphi)}), \quad (28)$$

Table 4
Summary of the MID Parameter Estimates for All the Considered Mass and Redshift Subsamples, Fitted on Planck Compton Profiles

Priors		Planck Parameter Estimates						
z	$M_{500}(M_{\odot})$	[2.0, 10.0]	[0.0, 3.0]	[0.0, 3.0]	[2.0, 6.5]	[0.1, 0.5]	[0.0, 12.0]	[0.0, 1.0]
		P_0	c_{500}	α	β	b_h	σ_{off} (arcminutes)	f_{off}
0.175	$10^{14.15}$	$6.4^{+2.2}_{-2.7}$	$2.2^{+0.5}_{-0.6}$	$2.1^{+0.6}_{-0.7}$	$5.1^{+1.0}_{-1.0}$	$0.3^{+0.2}_{-0.1}$	$2.9^{+0.9}_{-0.7}$	$0.7^{+0.2}_{-0.2}$
0.175	$10^{14.45}$	$5.2^{+3.3}_{-2.4}$	$1.7^{+0.7}_{-0.5}$	$1.7^{+0.8}_{-0.6}$	$4.8^{+1.2}_{-0.9}$	$0.2^{+0.2}_{-0.1}$	$3.2^{+0.9}_{-0.7}$	$0.8^{+0.1}_{-0.2}$
0.175	$10^{14.80}$	$5.1^{+3.0}_{-2.1}$	$1.9^{+0.7}_{-0.6}$	$1.9^{+0.7}_{-0.7}$	$4.7^{+1.2}_{-1.1}$	$0.3^{+0.2}_{-0.2}$	$3.4^{+0.8}_{-0.7}$	$0.8^{+0.1}_{-0.1}$
0.175	All M_{500}	$6.2^{+2.6}_{-2.6}$	$2.1^{+0.5}_{-0.5}$	$2.2^{+0.5}_{-0.7}$	$5.3^{+0.8}_{-0.9}$	$0.3^{+0.1}_{-0.1}$	$3.1^{+0.5}_{-0.5}$	$0.9^{+0.1}_{-0.1}$
0.525	$10^{14.15}$	$6.1^{+3.0}_{-2.7}$	$2.2^{+0.5}_{-0.6}$	$1.9^{+0.8}_{-0.9}$	$4.2^{+1.2}_{-0.9}$	$0.3^{+0.1}_{-0.1}$	$4.4^{+1.0}_{-1.0}$	$0.9^{+0.1}_{-0.1}$
0.525	$10^{14.45}$	$4.7^{+3.2}_{-2.0}$	$1.9^{+0.7}_{-0.7}$	$1.1^{+1.5}_{-0.5}$	$3.6^{+0.7}_{-0.4}$	$0.2^{+0.2}_{-0.1}$	$7.2^{+2.9}_{-2.8}$	$0.5^{+0.2}_{-0.4}$
0.525	$10^{14.80}$	$6.4^{+2.0}_{-2.8}$	$1.8^{+0.7}_{-0.7}$	$1.4^{+0.9}_{-0.6}$	$4.9^{+0.9}_{-0.8}$	$0.2^{+0.2}_{-0.1}$	$2.1^{+2.1}_{-1.4}$	$0.3^{+0.3}_{-0.2}$
0.525	All M_{500}	$5.5^{+2.8}_{-2.3}$	$1.9^{+0.7}_{-0.8}$	$1.6^{+0.8}_{-0.7}$	$4.1^{+1.6}_{-0.7}$	$0.3^{+0.1}_{-0.2}$	$4.3^{+0.8}_{-1.2}$	$0.8^{+0.1}_{-0.1}$
0.850	$10^{14.15}$	$5.9^{+2.8}_{-2.4}$	$2.0^{+0.6}_{-0.7}$	$1.8^{+0.9}_{-0.7}$	$4.8^{+1.2}_{-1.0}$	$0.3^{+0.2}_{-0.2}$	$2.9^{+3.5}_{-1.4}$	$0.5^{+0.3}_{-0.3}$
0.850	$10^{14.45}$	$6.0^{+2.9}_{-2.8}$	$2.1^{+0.6}_{-0.7}$	$1.5^{+1.1}_{-0.7}$	$4.2^{+1.3}_{-0.9}$	$0.3^{+0.1}_{-0.1}$	$4.6^{+2.4}_{-2.0}$	$0.6^{+0.2}_{-0.2}$
0.850	$10^{14.80}$	$5.6^{+3.1}_{-2.3}$	$2.2^{+0.5}_{-0.7}$	$1.6^{+0.9}_{-0.7}$	$5.0^{+1.1}_{-0.9}$	$0.3^{+0.1}_{-0.2}$	$4.1^{+5.9}_{-2.7}$	$0.3^{+0.3}_{-0.2}$
0.850	All M_{500}	$6.0^{+2.6}_{-2.3}$	$2.0^{+0.6}_{-0.8}$	$1.6^{+0.9}_{-0.7}$	$5.0^{+0.9}_{-1.1}$	$0.3^{+0.2}_{-0.2}$	$2.6^{+1.5}_{-0.8}$	$0.7^{+0.2}_{-0.3}$
All z	$10^{14.15}$	$5.7^{+2.6}_{-2.3}$	$2.0^{+0.6}_{-0.6}$	$1.9^{+0.8}_{-0.6}$	$5.0^{+0.9}_{-0.9}$	$0.3^{+0.2}_{-0.1}$	$3.3^{+0.5}_{-0.4}$	$0.9^{+0.1}_{-0.1}$
All z	$10^{14.45}$	$6.0^{+2.5}_{-2.2}$	$1.8^{+1.0}_{-1.0}$	$1.4^{+0.9}_{-0.7}$	$4.1^{+1.4}_{-0.9}$	$0.3^{+0.1}_{-0.1}$	$5.0^{+1.9}_{-1.7}$	$0.6^{+0.1}_{-0.2}$
All z	$10^{14.80}$	$6.8^{+2.8}_{-3.6}$	$1.9^{+0.6}_{-0.8}$	$1.6^{+1.0}_{-0.8}$	$5.2^{+0.7}_{-1.0}$	$0.2^{+0.2}_{-0.1}$	$2.3^{+0.6}_{-0.8}$	$0.7^{+0.2}_{-0.3}$
All z	All M_{500}	$5.9^{+2.3}_{-2.0}$	$2.0^{+0.7}_{-0.7}$	$1.8^{+0.7}_{-0.7}$	$4.9^{+1.2}_{-1.0}$	$0.3^{+0.1}_{-0.2}$	$3.2^{+0.5}_{-0.6}$	$0.8^{+0.1}_{-0.1}$

Note. The values are computed as the marginalized distribution medians; the error bars quantify the 68% confidence level.

i.e., by integrating a set of profiles whose center is located θ_{off} away from the nominal position, over all possible directions.

The value of the miscentering offset θ_{off} is generally not known a priori. Previous work has found that it reasonably follows a Rayleigh distribution with parameter σ_{off} (Johnston et al. 2007):

$$P(\theta_{\text{off}}, \sigma_{\text{off}}) = \frac{\theta_{\text{off}}}{\sigma_{\text{off}}^2} \exp \left[-\frac{1}{2} \left(\frac{\theta_{\text{off}}}{\sigma_{\text{off}}} \right)^2 \right], \quad (29)$$

so that the expected value for the offset is²⁹ $\theta_{\text{off}} \simeq 1.25 \sigma_{\text{off}}$. The mean miscentered profile $\bar{y}_{\text{off}}(\theta)$ can then be evaluated by averaging over all possible values of the miscentering, weighted by its probability distribution:

$$\bar{y}_{\text{off}}(\theta|\sigma_{\text{off}}) = \int_0^{\infty} d\theta_{\text{off}} P(\theta_{\text{off}}, \sigma_{\text{off}}) y_{\text{off}}(\theta|\theta_{\text{off}}). \quad (30)$$

In our analysis, both the miscentering offset σ_{off} and the fraction of miscentered profiles f_{off} are taken as free parameters.

As a very last step in our theoretical prediction, we subtract from the profile its zero level:

$$y_{\text{theo}}(\theta) = y_{\text{msc}}(\theta) - \bar{y}_{\text{bkg}}. \quad (31)$$

The background value \bar{y}_{bkg} is computed as the mean of the profile amplitude over the same θ range that was considered in Section 4.2, when computing the zero level for the profiles measured from the y-stacks.

6. Parameter Estimation

In this section, we present the results for the estimates of the pressure profile parameters.

²⁹ Hereafter, we shall refer to the parameter σ_{off} as the miscentering offset, although the real angular displacement is quantified by θ_{off} .

6.1. Methodology

The ultimate goal of this study is to provide novel estimates of the parameters entering the expression of the UPP in Equation (3). As our analysis is based on tSZ measurements alone, without the inclusion of numerical simulations or X-ray data, we do not fit for the central slope of the profile, which we fix to the fiducial value $\gamma = 0.31$, as has been done in similar tSZ-based works (Table 1). In addition, we fit for the hydrostatic mass bias b_h and the values of the miscentering offset σ_{off} and fraction f_{off} . Our parameter space is then seven-dimensional, with a generic parameter state Θ defined as the list of values

$$\Theta = \{P_0, c_{500}, \alpha, \beta, b_h, \sigma_{\text{off}}, f_{\text{off}}\}. \quad (32)$$

For a given set of the aforementioned parameters, the formalism described in Section 5 allows us to compute the associated profile $y(\Theta)$.

For each of the 16 cluster samples, we fit the theoretical prediction $y(\Theta)$ against the profile y^{obs} extracted from the stack. The best-fit parameters are defined as the set Θ_{bf} that maximizes the likelihood

$$\begin{aligned} \mathcal{L}(\Theta) &= \exp \left[-\frac{1}{2} (y(\Theta) - y^{\text{obs}})^T C^{-1} (y(\Theta) - y^{\text{obs}}) \right], \quad (33) \end{aligned}$$

where C is the covariance matrix measured for the chosen sample, as described in Section 4.2. In fact, due to the relatively high number of parameters, a direct maximization of the likelihood is not feasible; we adopt instead a Markov Chain Monte Carlo (MCMC) approach to explore the parameter space. Specifically, we employ the Python `emcee` package, which is an implementation of the affine invariant ensemble sampler from Goodman & Weare (2010). We adopt flat uninformative priors on all parameters; the associated ranges

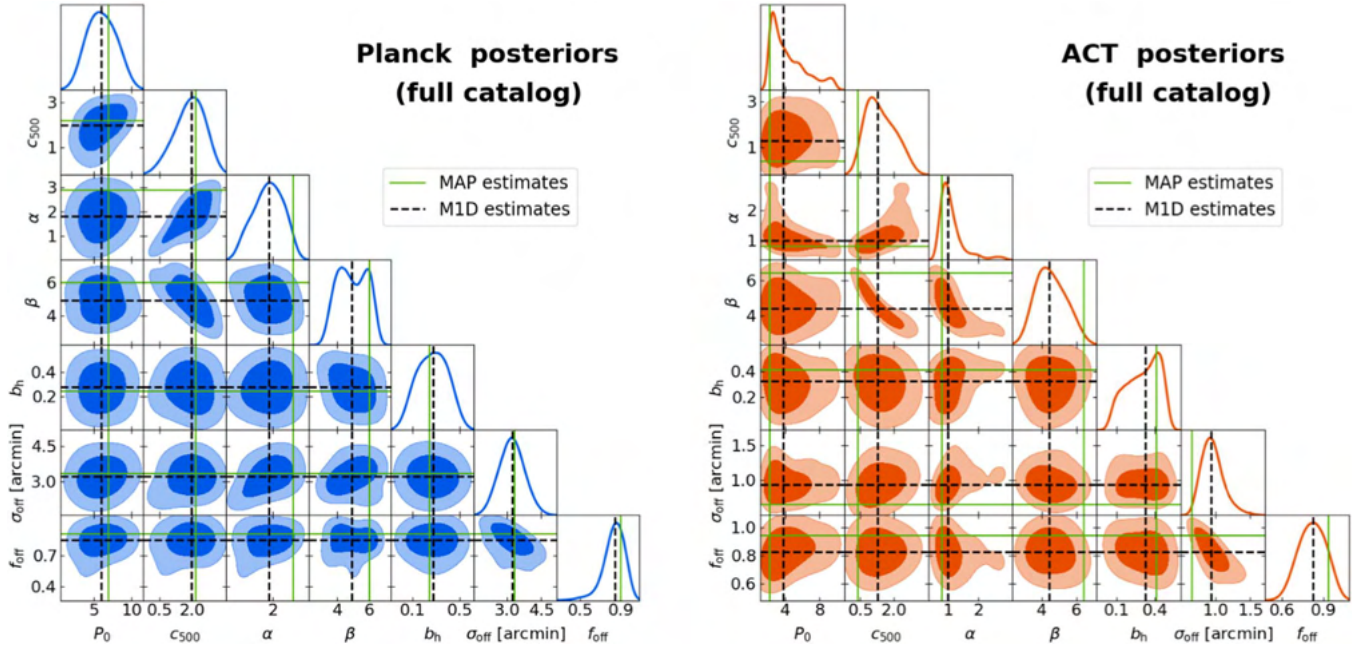


Figure 12. Posterior probability distributions for the model parameters, obtained by fitting our theoretical model to the profile corresponding to the stack of the full cluster catalog for Planck (left) and ACT (right). The posteriors are plotted as contours showing the 68% and 95% confidence levels. The solid green lines mark the highest-probability best-fit (MAP) values, while the dashed black lines mark the MID estimates computed from marginalized one-dimensional distributions.

Table 5
Summary of the MID Parameter Estimates for All the Considered Mass and Redshift Subsamples, Fitted on ACT Compton Profiles

Priors		[2.0, 10.0]	[0.0, 3.0]	[0.0, 3.0]	[2.0, 6.5]	[0.1, 0.5]	[0.0, 3.0]	[0.0, 1.0]
z	$M_{500} (M_{\odot})$	P_0	c_{500}	α	β	b_h	σ_{off} (arcminutes)	f_{off}
0.175	$10^{14.15}$	$5.1^{+3.0}_{-2.2}$	$2.0^{+0.7}_{-0.7}$	$1.6^{+0.8}_{-0.5}$	$4.2^{+1.0}_{-0.6}$	$0.3^{+0.1}_{-0.2}$	$1.8^{+0.3}_{-0.2}$	$1.0^{+0.0}_{-0.0}$
0.175	$10^{14.45}$	$4.2^{+3.1}_{-1.7}$	$1.9^{+0.6}_{-0.6}$	$1.9^{+0.6}_{-0.6}$	$4.5^{+1.1}_{-0.8}$	$0.3^{+0.1}_{-0.1}$	$1.8^{+0.5}_{-0.4}$	$0.7^{+0.1}_{-0.1}$
0.175	$10^{14.80}$	$5.0^{+3.0}_{-2.2}$	$2.0^{+0.6}_{-0.7}$	$1.5^{+0.7}_{-0.4}$	$4.2^{+1.0}_{-0.7}$	$0.3^{+0.1}_{-0.2}$	$1.7^{+0.5}_{-0.5}$	$0.6^{+0.1}_{-0.2}$
0.175	All M_{500}	$4.3^{+3.1}_{-1.7}$	$1.8^{+0.7}_{-0.6}$	$1.5^{+0.8}_{-0.5}$	$4.2^{+1.0}_{-0.6}$	$0.3^{+0.1}_{-0.2}$	$1.5^{+0.3}_{-0.2}$	$0.9^{+0.1}_{-0.1}$
0.525	$10^{14.15}$	$4.1^{+3.0}_{-1.6}$	$1.6^{+0.8}_{-0.7}$	$1.1^{+0.8}_{-0.4}$	$4.4^{+1.2}_{-0.9}$	$0.3^{+0.1}_{-0.2}$	$1.2^{+0.4}_{-0.3}$	$0.8^{+0.1}_{-0.1}$
0.525	$10^{14.45}$	$4.2^{+3.5}_{-1.7}$	$1.7^{+0.8}_{-0.7}$	$1.5^{+1.0}_{-0.6}$	$4.5^{+1.1}_{-0.8}$	$0.3^{+0.1}_{-0.2}$	$1.2^{+0.4}_{-0.5}$	$0.6^{+0.1}_{-0.1}$
0.525	$10^{14.80}$	$4.0^{+3.0}_{-1.5}$	$1.7^{+0.8}_{-0.6}$	$1.6^{+0.6}_{-0.4}$	$4.5^{+1.1}_{-0.8}$	$0.3^{+0.1}_{-0.2}$	$1.1^{+0.5}_{-0.4}$	$0.5^{+0.2}_{-0.2}$
0.525	All M_{500}	$4.2^{+3.0}_{-1.7}$	$1.3^{+0.9}_{-0.6}$	$1.0^{+0.6}_{-0.2}$	$4.6^{+1.1}_{-0.8}$	$0.3^{+0.1}_{-0.1}$	$1.0^{+0.3}_{-0.3}$	$0.7^{+0.1}_{-0.1}$
0.850	$10^{14.15}$	$5.0^{+3.1}_{-2.1}$	$1.8^{+0.8}_{-0.9}$	$1.3^{+0.8}_{-0.4}$	$4.3^{+1.4}_{-0.9}$	$0.3^{+0.1}_{-0.2}$	$0.9^{+0.5}_{-0.3}$	$0.8^{+0.2}_{-0.2}$
0.850	$10^{14.45}$	$5.4^{+2.9}_{-2.5}$	$2.0^{+0.7}_{-0.9}$	$1.2^{+0.7}_{-0.4}$	$4.2^{+1.0}_{-0.7}$	$0.3^{+0.1}_{-0.2}$	$0.7^{+0.5}_{-0.4}$	$0.5^{+0.3}_{-0.3}$
0.850	$10^{14.80}$	$4.6^{+3.0}_{-2.0}$	$2.3^{+0.5}_{-0.8}$	$1.4^{+0.8}_{-0.5}$	$4.6^{+1.1}_{-1.0}$	$0.3^{+0.1}_{-0.2}$	$0.8^{+1.4}_{-0.3}$	$0.6^{+0.3}_{-0.4}$
0.850	All M_{500}	$5.1^{+3.2}_{-2.5}$	$1.8^{+0.8}_{-0.7}$	$1.2^{+0.7}_{-0.3}$	$4.2^{+1.2}_{-0.7}$	$0.3^{+0.1}_{-0.2}$	$0.8^{+0.3}_{-0.2}$	$0.8^{+0.2}_{-0.2}$
All z	$10^{14.15}$	$4.5^{+2.9}_{-2.0}$	$1.8^{+0.8}_{-1.0}$	$1.1^{+0.6}_{-0.3}$	$4.0^{+1.4}_{-0.5}$	$0.3^{+0.1}_{-0.2}$	$1.1^{+0.2}_{-0.2}$	$0.9^{+0.1}_{-0.1}$
All z	$10^{14.45}$	$3.7^{+3.0}_{-1.3}$	$1.7^{+0.8}_{-0.6}$	$1.3^{+0.7}_{-0.4}$	$4.1^{+0.8}_{-0.5}$	$0.3^{+0.1}_{-0.2}$	$1.2^{+0.5}_{-0.4}$	$0.5^{+0.1}_{-0.1}$
All z	$10^{14.80}$	$3.4^{+4.3}_{-1.1}$	$1.6^{+0.7}_{-0.6}$	$1.4^{+0.6}_{-0.3}$	$4.4^{+1.1}_{-0.7}$	$0.3^{+0.1}_{-0.2}$	$0.9^{+0.4}_{-0.4}$	$0.5^{+0.2}_{-0.2}$
All z	All M_{500}	$3.8^{+2.9}_{-1.4}$	$1.3^{+0.9}_{-0.6}$	$1.0^{+0.4}_{-0.2}$	$4.4^{+1.1}_{-0.8}$	$0.3^{+0.1}_{-0.2}$	$0.9^{+0.2}_{-0.2}$	$0.8^{+0.1}_{-0.1}$

Note. The values are computed as the marginalized distribution medians; the error bars quantify the 68% confidence level.

are quoted in Tables 4 and 5. After burn-in removal and chain thinning, for each mass and redshift bin we are left with ~ 5000 samples of the posterior distribution on each parameter. The resulting joint probability contours for all parameter pairs, and the one-dimensional distributions for the individual parameters, are shown in Figure 12, for both Planck and ACT. The figure shows the results for the parameter estimation on the full

catalog; the posteriors for all the other $M-z$ bins are qualitatively similar, and are shown in Appendix B.

We consider two different approaches to determining the associated parameter estimates. First, we retrieve the septuple of parameters yielding the maximum value for the posterior probability distribution; we shall refer to these values as the maximum a posteriori (MAP) estimates. Since we are using flat

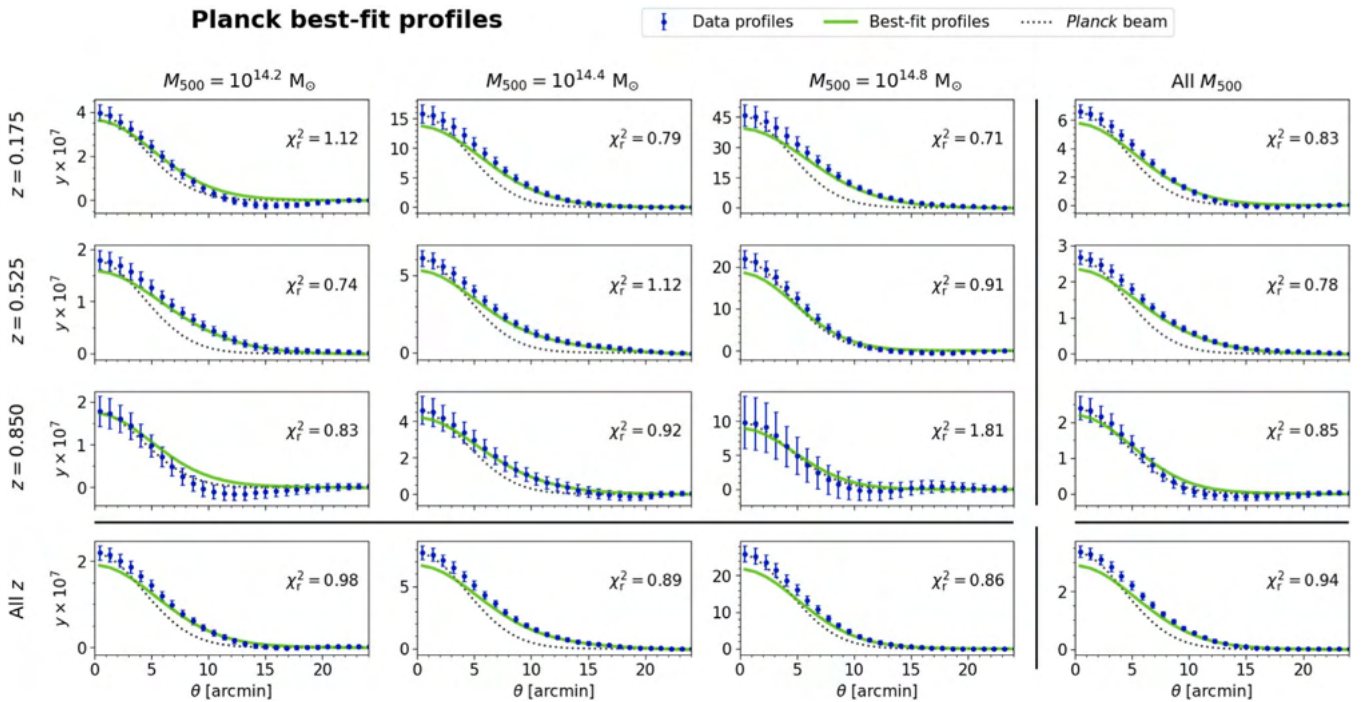


Figure 13. Comparisons between the Compton profiles measured on the Planck y-map (data points) and the theoretical profiles (solid lines) computed by adopting the best-fit (MAP) parameter values, for all the (M_{500}, z) cluster samples considered in this analysis. The plots also show, for reference, the Planck beam profile (dashed line), and quote the reduced chi-squared values.

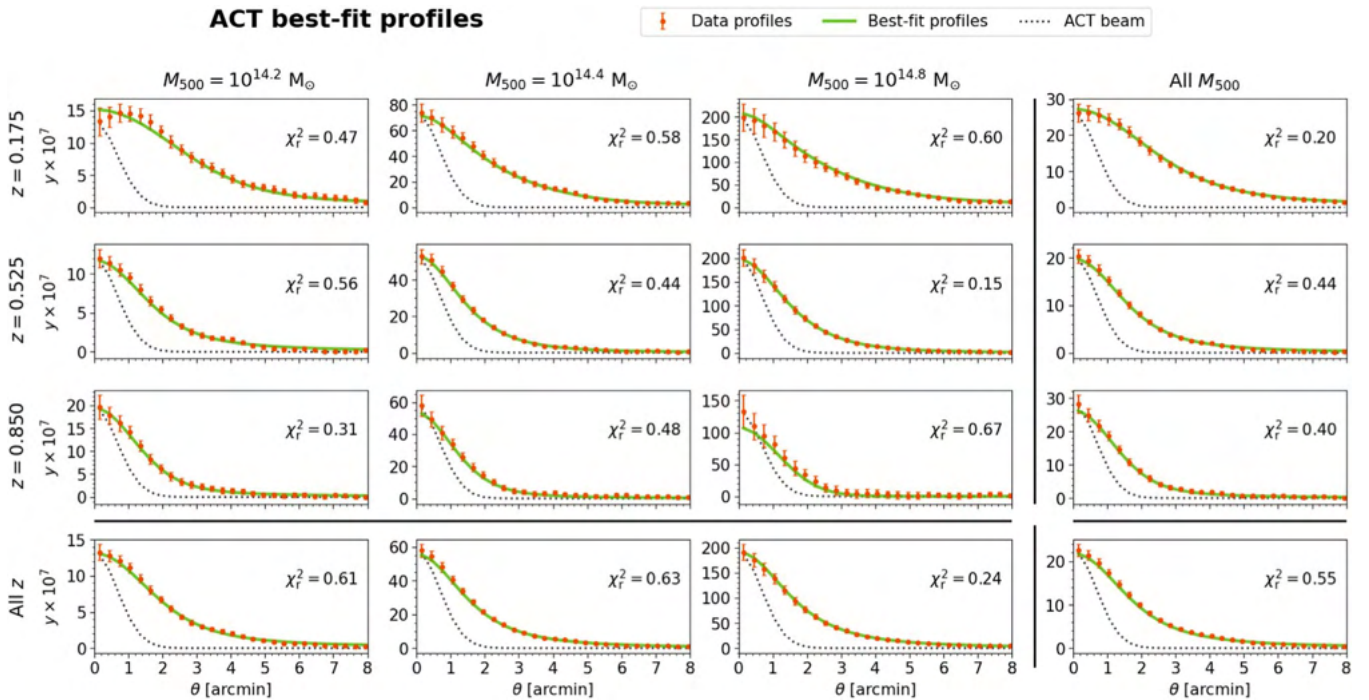


Figure 14. The same as Figure 13, but for the ACT profiles.

priors, the maximum of the posterior distribution also corresponds to the maximum of our likelihood from Equation (33), or, in other words, the MAPs are by definition our best-fit values Θ_{bf} . Second, we consider the estimates computed for each of the individual parameters as the 50th percentiles over their marginalized one-dimensional posterior distributions (i.e., the distributions plotted along the diagonals of the triangular plots in Figure 12 and similar); the associated

lower and upper error bars are evaluated as the separations from the 16th and 84th percentiles of the distribution, respectively. We shall refer to the resulting values as the marginalized one-dimensional (M1D) estimates.

In general, the MAP and M1D estimates do not necessarily agree. In fact, in situations involving a large number of parameters with nonlinear degeneracies, as is the case with our model, they are expected to show important differences (for an

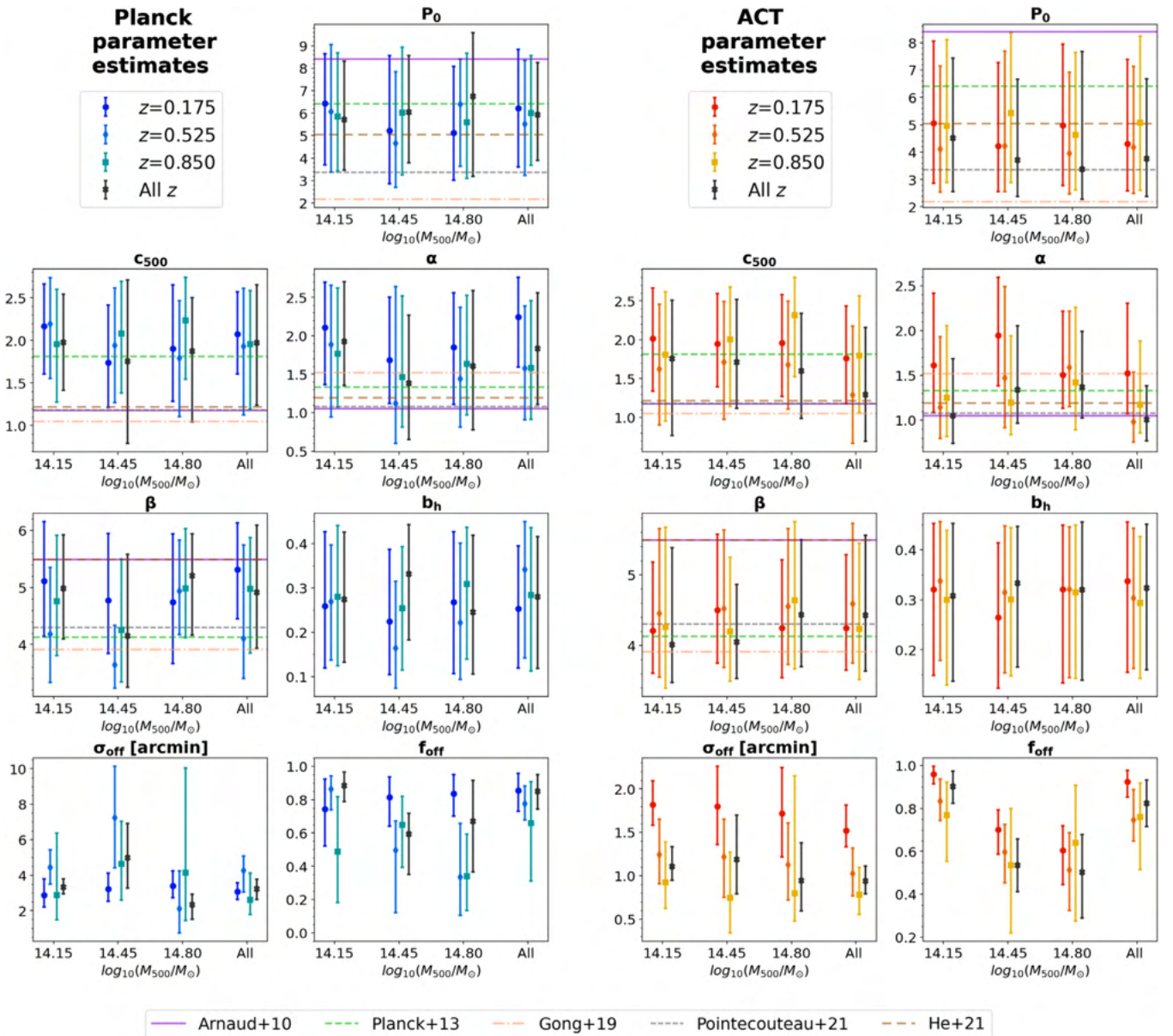


Figure 15. Final estimates on our model parameters, computed as the MID values for the marginalized distributions, obtained from the Planck (left) and ACT (right) stacks. Each panel shows the results for an individual parameter, grouping the estimates by mass bin, with the different redshift bins being shown by the different colors and markers, as detailed in the legends. We also include, in each panel, estimates of the considered parameter obtained from previous works, marked by the solid horizontal lines, color coded as detailed at the bottom of the figure.

extensive discussion, see, e.g., Section 6 in Joachimi et al. 2021). This is clearly visible in Figure 12, where the MAPs are shown by the solid green lines and MIDs by the dashed black lines. The two sets of parameters carry different information. The MAPs are our best-fit values, and are employed to compute the associated best-fit predictions for the Compton parameter profiles. The comparisons with our measurements are shown for all M - z bins in Figure 13 for Planck and Figure 14 for ACT. The MIDs, instead, quantify our fiducial 68% confidence levels on the individual parameters according to their final probability distributions, and can be compared with estimates from other works. The MIDs with associated error bars are quoted in Table 4 for Planck and Table 5 for ACT; they are also plotted in Figure 15, where it is possible to visualize their dependence on the selected mass and redshift bin.

As anticipated in Section 3.4, we also conduct an analogous parameter estimation analysis on the y -profiles obtained from

the merged catalog without any explicit mass rescaling. Hereafter, we shall refer to such profiles as “unscaled,” while we shall refer to the profiles shown in Figure 10 as “fiducial.” In Figures 16 and 17, we show, for Planck and ACT, respectively, a comparison between the fiducial and unscaled profiles, together with the theoretical predictions obtained by using the parameters fitted on the latter. Figures 18–22 show the posterior distributions for both the fiducial and unscaled profiles. As the focus in these figures is on the comparison between the two different sets of contours, we do not mark the locations of the associated MAP and MID estimates, to avoid excessive cluttering.

6.2. Discussion of the MCMC Results

We begin by commenting on the posterior probability contours plotted in Figure 12 and in Figures 18–22. The main

feature in these plots is the asymmetry in the shape of most of the probability contours. This is a direct result of the complexity of the model that we are fitting, and of the strong degeneracy that exists between the UPP parameters. Even though the chains are converged (in MCMC terms, the thinned chains are more than 50 times longer than their autocorrelation length), existing correlations between different parameters produce strong elongations of the contours and yield rather asymmetric posteriors for most of them. Notice that, when fitting this kind of model, this is not an unusual situation, as can be seen from, e.g., Figures 5 and 7 in G19; especially in the case of ACT, the shapes of our posterior distributions on P_0 , c_{500} , α , and β mimic the ones presented in that work. In the case of Planck, however, the contours are slightly larger and their shapes are more regular, which is most likely a result of the smoothing effect induced by the beam and the resulting extended correlation between neighboring θ bins. The higher resolution of ACT instead results in tighter contours and in a better quality fit overall.

In this context, the difference between the MAP and MID estimates becomes evident. We have verified that a choice of larger priors would yield poorer fitting results for both Planck and ACT: for very extended priors, the complex nature of the model leads the chains to encounter local likelihood maxima in positions of parameter space where the actual values of the individual parameters are rather unphysical. As a result, not only would the chains not reach a proper convergence, but the final posteriors, obtained by the merged contributions of these local maxima, would also be artificially broadened and lead to unrealistic MID estimates. The MAPs, by construction, would still yield best-fit profiles that match the data, but they would not necessarily have a real physical meaning; their combined numerical values would simply be effective in generating predictions that match our measurement, but due to the degeneracies in our model, different numerical sets could also provide good agreements with the data. A physical interpretation of the results therefore requires our MID estimates and their posterior distributions. In principle, in order to improve the chain convergence, we could impose Gaussian priors on some of the parameters (e.g., on c_{500} , which typically shows the strongest correlations), based on previous results. We have verified that Gaussian priors with typical uncertainties as found in the literature would override the constraining power of the chains and yield posteriors that resemble the chosen prior distributions. In order to keep our analysis independent from previous works, we maintain flat priors, chosen with a reasonable width in order to encompass other estimates from the literature and, at the same time, to ensure the good convergence of our Markov chains. Clearly, this choice has an effect on the resulting MID estimates, but it is still less obvious than imposing explicit Gaussian priors.

The plots in Figures 13 and 14 show that the models computed using our MAP parameters are effective in reproducing the measured profiles across the considered θ range. The figures also report, for each case, the associated reduced chi-squared value, defined as $\chi_r^2 = \chi^2/N_{\text{dof}}$, where $\chi^2 = -2 \ln \mathcal{L}$ with \mathcal{L} from Equation (33), and the number of degrees of freedom N_{dof} is computed as the number of angular bins employed in the fit minus the number of free parameters. In the case of ACT, we always have $\chi_r^2 < 1$, which proves the good agreement between the predictions and data. In the case of Planck, we generally have higher values and, for some bins,

$\chi_r^2 > 1$; a slight offset of the prediction with respect to the data is also visible in some of the plots. Once more, this effect has already been observed in the literature (e.g., Figure 6 in G19). In our case, the offset could be a result of the larger Planck beam; the latter, indeed, tends to regularize the bootstrap profiles and reduce their scatter around the mean, probably leading to an underestimation of the errors (for the same reason, the significances quoted for our measurements in Table 3 are always higher for Planck than for ACT). Besides, a larger beam implies more important correlations between neighboring angular bins. These two effects result in a decrease of the relative importance of the diagonal elements in the covariance matrix compared to the off-diagonal entries (as can also be appreciated from the correlation plots in Figure 11). At the parameter estimation level, this can produce the observed offsets in the Planck best-fit profiles.

We now turn our attention to the MID estimates, and to the effects of mass and redshift on their values. Figure 15 provides a comprehensive summary, which shows the trend of each parameter when changing M_{500} (the different positions in each panel) and z (the different colors and marker shapes of the points). The most striking feature in these plots is the fact that, regardless of the choice of mass or redshift bin, all estimates of the UPP parameters are compatible within 1σ . This observation, combined with the good agreement between the best-fit predictions and our measurements, suggests that the UPP is indeed successful in modeling the ICM electron pressure over the mass and redshift ranges spanned by our cluster sample. Still, Figure 15 shows that there are indeed mild variations for the parameters when changing M_{500} or z . Such variations, however, generally lack a consistent trend, so they provide no evidence of an effective mass or redshift residual dependence on the UPP parameters. Most likely, this is again a result of the model degeneracy, which also produces the rather large error bars on our estimates. Another feature corroborating this hypothesis is the fact that the marginalized cluster samples have often values that are not in between the ones obtained from the individual bins. We then conclude that the observed variations in the estimates for the different M - z bins are just a result of our parameter estimation, and not evidence of a real residual dependence of the UPP parameters on mass or redshift. We also find substantial agreement (within the error bars) between the Planck-based and ACT-based estimates of the UPP parameters.

6.3. Discussion of the Best-fit Estimates

We can now compare our findings with the values obtained from previous studies. Figure 15 overplots on each panel a few horizontal stripes to mark the locations of the results obtained from some of the works listed in Table 1. We observe that our estimates are in general compatible with these previous results. The only exception is the slope at intermediate radii α , for which, in the case of Planck, we obtain somewhat larger values. We stress, however, that in G19 some of the considered redshift bins yielded even larger values for α , up to 6 in the most extreme case. This large scatter of the estimates obtained from different studies is again the result of the existing degeneracies between the UPP parameters. We conclude that our estimates confirm the results from previous works; the sizes of our error bars are also comparable with the uncertainties quoted in the literature (when available; see again Table 1).

We comment that studies based on hydrodynamical simulations have also provided insights into the possible mass and redshift evolutions of the UPP parameters. The work presented in Battaglia et al. (2012) suggested that P_0 , c_{500} , and β require explicit mass and redshift dependencies in order to fit their simulation results (see Table 1 in that work for details); the analysis in Le Brun et al. (2015) also confirmed the mass dependence of P_0 and c_{500} , finding that both parameters increase with M_{500} (Table 2 in that work). The mass range explored in these works encompasses the range that we probe with our cluster sample. We stress, however, that the mass and redshift dependencies detected in those studies are in all cases very mild, and can only be measured with the high resolution provided by numerical simulations. In fact, the works of Battaglia et al. (2012) and Le Brun et al. (2015) probe the cluster pressure profile down to radial separations of $r \sim 0.04 R_{200}$ (Figures 1 and 2 in the former) and $r \sim 0.1 R_{500}$ (Figure 3 in the latter), respectively; for our lowest-redshift and highest-mass clusters, these values translate into angular scales of the order of $\sim 1'$, which, even for ACT, are comparable with the beam, and where we typically have the largest uncertainties in our profile measurements. Hence, the mass and redshift variations in the UPP parameters are definitely subdominant in the context of reconstructing the pressure profile from real data, due to a series of factors, such as the instrumental beam, residuals in the y -map, systematics in the cluster mass estimates, and miscentering effects. As far as our measurements are concerned, if an effective dependence of the UPP parameters on M_{500} and z does exist, it is well below the uncertainties in our final estimates.

We move on now to comment on our results for the hydrostatic mass bias b_h . Our estimates are typically in the range from 0.2 to 0.3, with somewhat larger values obtained with ACT; the confidence intervals are in any case quite broad, with typical error bars up to ~ 0.2 , and no evident strong degeneracies with the other parameters. A number of different estimates for b_h have been provided in the literature; for a summary, see, e.g., Table 3 in Ibitoye et al. (2022). Our results are again in agreement with previous findings. The numerical simulation results tend to agree that the hydrostatic bias has a mass dependence, and that it can accommodate values for b_h as large as 0.3, for massive clusters (Pearce et al. 2020; Barnes et al. 2021). Our findings are also in agreement with cross-correlation analyses (Makiya et al. 2020; Rotti et al. 2021; Ibitoye et al. 2022) and studies of variously selected cluster samples (von der Linden et al. 2014; Hoekstra et al. 2015; Sereno et al. 2017; Ferragamo et al. 2021; Aguado-Barahona et al. 2022). We stress, however, that our MCMC analysis does not provide strong constraints on the hydrostatic bias.

Finally, the miscentering parameters are the ones that show the largest scatter across different M - z bins. In this case, a comparison between Planck and ACT is not meaningful, as we set different priors on σ_{off} to account for the considerably different beam sizes. We find values for σ_{off} of around $4'$ in the case of Planck and of around $1.5'$ in the case of ACT; for the latter, the miscentering offset is then comparable with the beam's FWHM, and is therefore a relatively more important effect, as expected. As for the miscentering fraction f_{off} , we find in general that more than 50% of the clusters in each sample are offset from their nominal positions; a mild anticorrelation can be observed between σ_{off} and f_{off} in Figure 12, which is easily understandable, as these parameters produce opposite effects in

quantifying the mean miscentering. We also notice from Figure 15 that, this time, it is possible to recognize a trend in the MID values, especially for ACT, with lower redshifts and lower masses requiring a higher miscentering offset. This could have been anticipated by looking at the stacks plotted in Figure 8, where the lowest masses and redshifts tend to have broader and more irregular profiles. These results confirm that the miscentering is a necessary inclusion in our theoretical modeling, without which the final estimates on the other UPP parameters would most likely be biased. For example, we found that when we did not include the miscentering in our theoretical prediction, the resulting estimates on the parameter P_0 were typically very low and unphysical ($P_0 \lesssim 2$); this can be understood, as P_0 is the parameter that most directly controls the amplitude of the measured signal, and, as such, most readily absorbs any dilution effect that is produced by the miscentering on the profiles.

Before closing this section, we comment on the effect that the mass rescaling that we applied to the WHL and DESI clusters had on our parameter estimates. Figures 18–22 show the comparisons between the final contours obtained from our fiducial profiles and from the unscaled profiles, for all M - z bins and for both Planck and ACT. The resulting best-fit predictions for the unscaled profiles (computed based on the associated MAP estimates) are overplotted on the profiles themselves in Figures 16 and 17. Regarding the agreement between the predictions and the measurements for the unscaled profiles, similar considerations as for the case of the fiducial profiles apply. As for the final MID parameter constraints, it is clear from the contour plots that the posteriors for the unscaled profiles are almost indistinguishable from the posteriors obtained for the fiducial profiles. Even for the case of the lowest-redshift bin, where the two sets of profiles show the largest tensions, the final parameter estimates are rather compatible. This shows once more that the final contour sizes are largely determined by our prior choice and by the correlation between the parameters entering our model; such correlations also result in large error bars and cause the estimates to be in agreement overall. Clearly, the actual final MID values are not exactly the same, and one could quote the difference between them as a systematic error component to be included in our final parameter uncertainties. In our case, however, such a systematic contribution will be much smaller than the statistical uncertainties quoted in Tables 4 and 5. We then conclude that the mass rescaling presented in Section 3.4 has a negligible impact on the final conclusions of this study.

7. Conclusions

The cluster pressure profile is one of the primary tools for exploring the physical state of the ICM; as is clear from Equation (2), the Compton parameter y is a very direct probe of the ICM electron pressure, and it has been exploited in this way by several works over the past decade. In this paper, we have explored the possible mass and redshift dependencies of the parameters governing the shape of the UPP in galaxy clusters, by analyzing the y -profiles obtained from cluster stacks on Compton parameter maps.

We employed the y -maps delivered from both the Planck satellite and the ACT, the latter limiting the analysis to an effective sky area of $\sim 2000 \text{ deg}^2$, but at the same time providing a considerably higher angular resolution for the reconstructed tSZ signal. We built a large cluster sample, by

merging existing galaxy cluster catalogs based on observations from KiDS, SDSS (WHL), and DESI. As the cluster masses from these catalogs were estimated by following different methodologies, we first homogenized the mass definition, by scaling the WHL and DESI cluster masses to the KiDS definition, which is based on WL measurements and, as such, is less affected by ad hoc assumptions of the ICM’s physical state. The scaling parameters were obtained by comparing the masses from common clusters across pairs of catalogs, for different redshift intervals. After applying a lower mass cut of $10^{14} M_{\odot}$ (below which we found that the stacks would become too noisy), and removing repeated clusters, we merged the three catalogs, obtaining a final sample of 23,820 clusters overlapping with the ACT map footprint.

We split these clusters into three mass and three redshift bins, also considering the respective marginalized cases, for a total of 16 different cluster samples. We stacked these samples on both the Planck and ACT maps, in all cases obtaining a clear detection of the cluster signal against the background. We extracted a circularly symmetric radial angular profile from each stack map, and computed the associated covariance matrix, by repeating the stacks with a set of 500 replicas of the catalog obtained via bootstrap resampling. The covariance matrices allowed us to determine the uncertainties that were to be assigned to the angular profiles and to compute the significance per bin for their measurements, which was always larger than 13 for Planck and 3 for ACT.

We theoretically modeled the mean y -profile with a halo model approach, taking into account the effective cluster mass and redshift distributions in each sample. The theoretical predictions depend not only on the UPP parameters, but also on the hydrostatic bias on the cluster mass, and on two parameters quantifying the magnitude and occurrence of the possible miscentering of the clusters from their nominal positions. We then employed the MCMC method to reconstruct the posterior distributions on these parameters with initial flat priors, where the likelihood compares the theoretical prediction with the observed profile, using the covariance matrix measured for each cluster sample. In all cases, we fixed the pressure profile’s central slope to $\gamma = 0.31$, as is customary in other works based on tSZ data alone. From the MCMC runs, we extracted two sets of parameters: the MAPs from the full seven-dimensional likelihood and the MIDs from the marginalized one-dimensional posteriors.

The profile predictions computed with the MAPs provided a good fit to our measurements, yielding $\chi_r^2 < 1$ for almost all cases. The MID estimates showed good agreement between Planck and ACT, and with the constraints obtained by previous works. The results also do not show any compelling evidence for the residual dependence of the UPP parameters on either M_{500} or z . Although marginal differences are visible, there are no clear trends, and the values are largely compatible within the recovered error bars. The main conclusion from this work is that the adopted UPP functional form is effective in describing the ICM electron pressure profile for clusters in the mass range ($10^{14.0} M_{\odot} < M_{500} < 10^{15.1} M_{\odot}$) and in the redshift range ($0.02 < z < 0.97$), as explored with our clusters. This is the first time that the UPP has been tested over such a large cluster sample, which is mostly complete within the chosen M_{500} and z limits. We also obtain loose constraints on the hydrostatic mass bias, in agreement with previous works, based on both numerical simulations and analyses of cluster samples. We

prove that miscentering is an important element in cluster profile modeling, with more than 50% of the clusters being offset from their nominal positions by amounts commensurate with the FWHM values of the corresponding y -maps. Finally, we have shown that the possible systematic errors induced by our explicit mass rescaling are well below the statistical uncertainties obtained for each parameter from the MCMC analysis.

We would like to thank Yan Gong, Zhong-Lue Wen, Joachim Harnois Deraps, and Xiaohu Yang for their useful discussions. Based on data products from observations made with ESO Telescopes at the La Silla Paranal Observatory under program IDs 177.A-3016, 177.A-3017, and 177.A-3018, and on data products produced by Target/OmegaCEN, INAF-OACN, INAF-OAPD, and the KiDS production team, on behalf of the KiDS consortium. OmegaCEN and the KiDS production team acknowledge support from NOVA and NWO-M grants. The members of INAF-OAPD and INAF-OACN also acknowledge the support from the Department of Physics & Astronomy of the University of Padova and the Department of Physics of University Federico II (Naples). D.T. acknowledges support from the Chinese Academy of Sciences (CAS) President’s International Fellowship Initiative (PIFI), under Grant No. 2020PM0042, and from the National Natural Science Foundation of China (NSFC) Research Fund for International Scientists (RFIS), under Grant No. 12150410315. Y.Z.M. acknowledges support from the National Research Foundation, under grant Nos. 120385 and 120378, and a SARAO group grant. Project 12047503 is supported by the National Natural Science Foundation of China. This work was part of the research program “New Insights into Astrophysics and Cosmology with Theoretical Models Confronting Observational Data,” of the National Institute for Theoretical and Computational Sciences of South Africa. Z.Y. acknowledges support from the Max Planck Society and the Alexander von Humboldt Foundation in the framework of the Max Planck-Humboldt Research Award endowed by the Federal Ministry of Education and Research (Germany). C.G. and L.M. acknowledge the support from the grant PRIN-MIUR 2017 WSCC32 ZOOMING as well as the support from the grant ASI n.2018-23-HH.0. C.G. acknowledges funding from the Italian National Institute of Astrophysics, under the grant “Bando PrIN 2019,” PI: Viola Allevalo. A.H.W. is supported by a European Research Council Consolidator grant (No. 770935). M.S. acknowledges financial contributions from contract ASI-INAF n.2017-14-H.0 and contract INAF mainstream project 1.05.01.86.10.

Appendix A Summary of Previous Works

We provide here further information about the previous results for the UPP parameters, as a continuation of the discussion presented in Section 1. We focus in particular on the cluster-based studies that are listed in Table 1.

The work in Arnaud et al. (2010) considered 33 clusters with $M_{500} \in [1, 10] \times 10^{14} M_{\odot}$ at $z < 0.2$, observed by XMM-Newton, and compared their individual pressure profiles, each scaled by the characteristic pressure P_{500} ; these clusters were selected from the REFLEX Cluster Survey, by imposing a lower X-ray luminosity threshold of $0.4 \times 10^{44} h^{-2} \text{ erg s}^{-1}$ in the 0.1 – 2.4 keV band (the REXCESS sample; Böhringer et al.

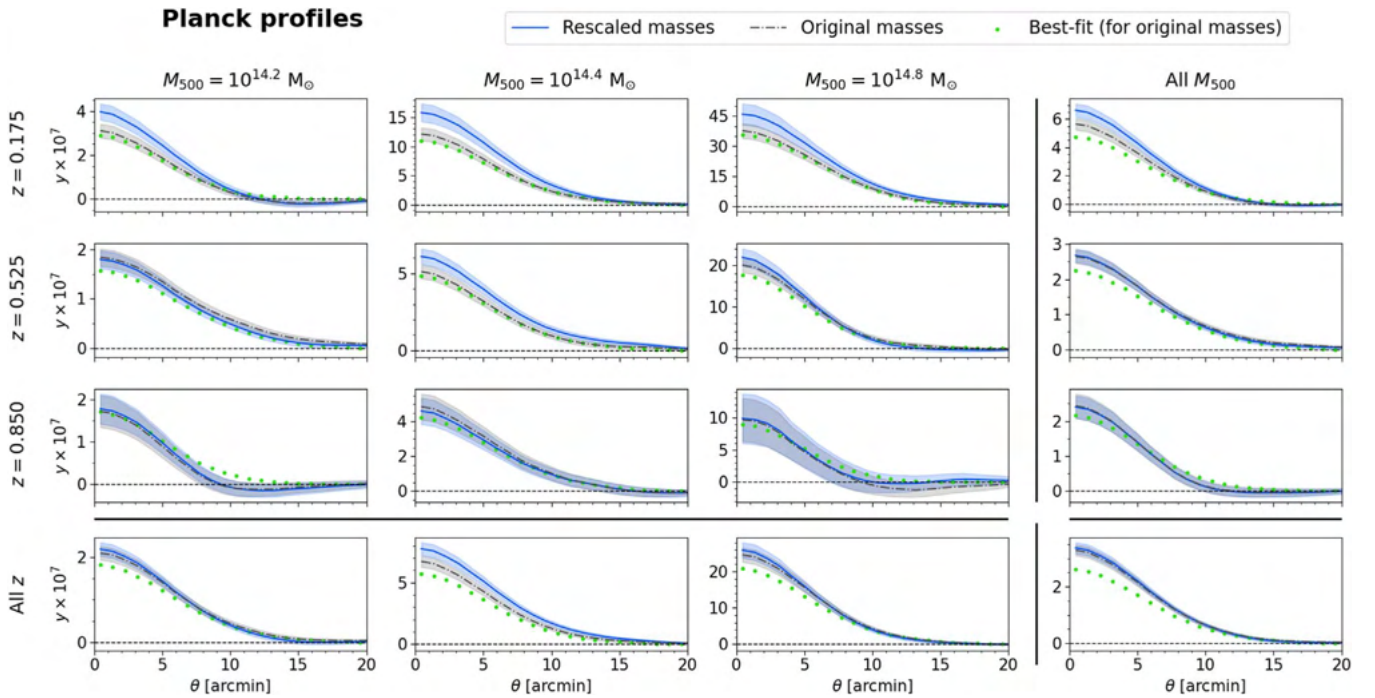


Figure 16. Comparisons between the angular y -profiles measured on the Planck map with the fiducial sample (blue) and the unscaled sample (gray). For both cases, the shaded areas quantify the associated uncertainties. The green dots show the model predictions for the unscaled profiles, computed using the MAP estimates from the associated MCMC runs.

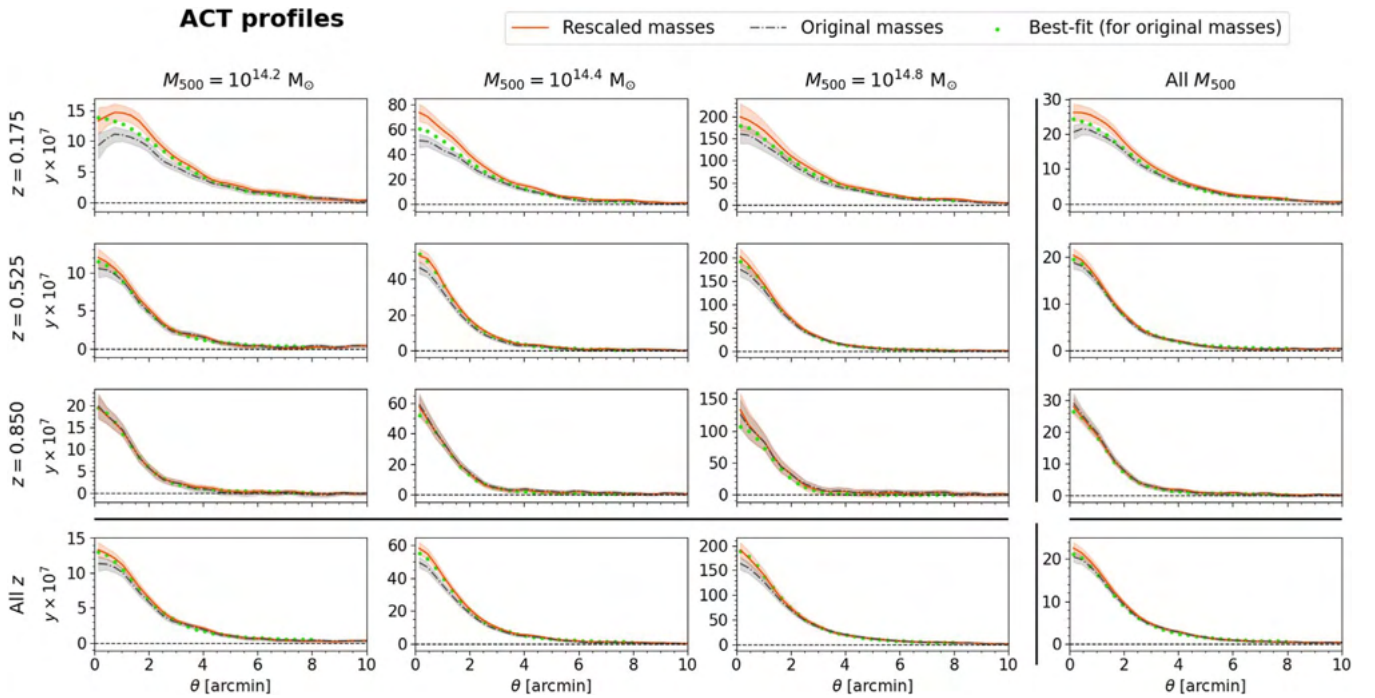


Figure 17. The same as Figure 16, but for the profiles measured on the ACT map. The profiles obtained with the fiducial sample are this time plotted in red.

2007). REXCESS is by construction a representative sample of an X-ray flux-limited cluster population, which does not privilege specific morphologies or dynamical states in its member clusters. Although deviations between cool-core and morphologically disturbed systems in the central region were found, the scaled profiles in Arnaud et al. (2010) showed good agreement at larger radii, up to R_{500} . The UPP parameters were fitted to a combination of the mean X-ray data profile and the

mean profile obtained from numerical simulations, with the latter allowing the profile reconstruction to be extended beyond R_{500} . This work has traditionally been taken as a point of reference for all subsequent studies of cluster pressure profiles.

A similar analysis was conducted by the Planck Collaboration et al. (2013) on a set of 62 tSZ-detected clusters with $M_{500} \in [2, 20] \times 10^{14} M_{\odot}$ at $z < 0.45$; this cluster sample had already been used to calibrate the tSZ–mass scaling relation in

Planck Collaboration et al. (2011b), where it was selected from the Planck early SZ source catalog (Planck Collaboration et al. 2011a) on the basis of existing high-quality XMM-Newton observations. This time, information about the pressure profile was obtained from the reconstructed cluster Compton profile, which allowed the authors to explore the ICM gas out to $\sim 3 R_{500}$; the average derived pressure profile was combined with the average profile obtained from X-ray data. The inclusion of X-ray data allowed the reconstruction of the pressure profile down to $0.02 R_{500}$, yielding substantial agreement with the SZ data in the overlap range. Again, marginal differences were observed between cool-core and non-cool-core clusters, but within the statistical error bars. Compared with the results from numerical simulations, the profile for the cluster outskirts was found to be flatter, while providing good agreement at low radii with simulations that implement feedback from active galactic nuclei.

The work in Sayers et al. (2016) considered a set of 47 clusters with $M_{500} \in [3, 25] \times 10^{14} M_{\odot}$ at $z < 0.9$, chosen from observations with Chandra and Bolocam (Sayers et al. 2011), on the basis of their redshifts and high X-ray temperatures; this sample slightly extended the one that had already been studied in Czakon et al. (2015), by including two additional clusters. This work focused on the reconstruction of the pressure profile for the cluster outskirts, based on measurements of the integrated y -profile from Bolocam and Planck data. More precisely, all UPP parameters were fixed to the Arnaud et al. (2010) estimates, with the exception of the normalization P_0 and the profile slope β at large radii. The best-fit values were found to be in agreement with the results from numerical simulations over the same mass and redshift span of the considered cluster sample. The authors also found evidence for a residual mild dependence of the profile slope on the cluster mass, with more massive clusters favoring higher values of β . Finally, the work acknowledged how these results can be affected by systematics, such as sample selection and the calibration of cluster masses.

In Pointecouteau et al. (2021), the cluster sample consisted of 31 clusters with $M_{500} \in [3.4, 13.1] \times 10^{14} M_{\odot}$ at $z < 0.71$, which had been previously listed as SZ sources in both Planck- and ACT-based catalogs. A major novelty of this work is that the SZ signal was measured on a joint Planck–ACT Compton parameter map, built from a linear combination of the individual frequency maps resulting from the two surveys, as described in Aghanim et al. (2019). The authors extracted y -profiles (and derived the associated pressure profiles) for individual clusters in the sample, then fitted the resulting mean pressure profile with a UPP model. As the fitting results were strongly affected by parameter degeneracies, the authors fixed both γ and c_{500} to the values from Arnaud et al. (2010). Estimates for the remaining UPP parameters showed broad agreement with previous findings, particularly when it came to the profile amplitude at outer radii, while a somewhat larger tension was found for intermediate radii; the authors mentioned the higher relevance of the ACT data (a novelty in this analysis) in this radial range as a possible explanation, while stressing again the limitations that were inherent to the use of a relatively small nonrepresentative sample.

Finally, He et al. (2021) employed the same cluster sample (REXCESS) as in Arnaud et al. (2010), and focused on assessing the effects on scaling relations and UPP parameter estimates deriving from the bias between the true cluster mass

and the hydrostatic cluster mass as sampled by X-ray and SZ observations (see also Section 5.1), an issue that had already been acknowledged in Arnaud et al. (2010). The authors fitted the scaling between the two mass definitions on hydrodynamic simulations and employed it to correct the cluster masses in the REXCESS sample, finding that the initial hydrostatic mass values were underestimated by 7%, on average, the effect being larger for higher masses. The scaling was then quantified via a hydrostatic mass bias and incorporated into the formalism by scaling the UPP normalization pressure P_0 and concentration c_{500} (this is equivalent to our treatment of the bias, as described in Section 5.1, with the difference that we kept the UPP functional form unchanged and scaled the values of M_{500} and R_{500} instead). The authors fitted this modified UPP model to the new mean pressure profile, finding the resulting prediction to yield a reduction in the deviation (quantified by the term in Equation (14)) from the self-similar model, compared to the original UPP profile.

The list of studies described in this section, together with the summary reported in Table 1, are by no means exhaustive; as the present paper is not intended to provide a review of the subject, we redirect readers to the additional references cited in those works for further reading. We choose to present and discuss this particular selection of papers in order to highlight the novel aspects that are introduced by each of them, namely the systematic application of the UPP to cluster pressure profiles derived from X-ray data (Arnaud et al. 2010), the extension of a similar study to profiles reconstructed from SZ data (Planck Collaboration et al. 2013), considerations of the possible mass and redshift dependencies of the UPP parameters (Sayers et al. 2016), the introduction of ACT data (Pointecouteau et al. 2021), and the importance of the hydrostatic mass bias (He et al. 2021). All of these aspects are also considered in our data analysis and theoretical modeling; the change in approach, from considering a reduced number of clusters to reconstructing the statistical properties of an extended sample, as in G19, is particularly relevant, however, and is therefore described in the main text in Section 1.

Looking back at Table 1, the best-fit numerical values resulting from these studies show a large scatter. Two main factors contribute to the observed differences. First, the UPP parameters are intrinsically degenerate, as is clear from the functional form in Equation (3); this implies that different combinations of parameter values can provide equally effective predictions for the observed pressure profiles. A possible way of circumventing this issue, as adopted by Sayers et al. (2016) and Pointecouteau et al. (2021), for example, is to keep some of the parameters fixed in the analysis, which comes at the price of a slight loss in the generality of the fitted model. In our study, we choose, in a more bias-free approach, as in G19, to keep all parameters free, with the exception of the inner slope γ , as is customary in purely SZ-based analyses. Still, we acknowledge that parameter degeneracy is an important issue, and as such it is extensively addressed in our discussion of the fit results in Sections 6.2 and 6.3.

The second main reason for the scatter that is observed in Table 1 is because whenever the chosen sample is restricted to a handful of clusters that are well resolved and characterized by observations at different wavelengths, the results of the UPP estimates are inevitably subject to potential selection biases. This is generally acknowledged in the studies described in this section. In particular, it is worth stressing that the cluster

samples that are constructed on the basis of existing high-quality data in ancillary studies are nonrepresentative, which prevents the conclusions from the corresponding studies being extended to a generic cluster with mass and redshift in the sample span. The only exceptions from the above list are the works based on REXCESS, which was purposely built as a representative sample. The cluster sample used in this work is not only representative (as it includes all clusters with estimated masses above a common threshold), but also complete (typically $>90\%$; see Section 3), which is a fundamental difference compared to the previous studies. The possible dependencies of the UPP parameters on cluster mass and redshift actually constitute one of the core topics of our analysis, and this is explored by binning our cluster sample in different M_{500} and z bins, as detailed in Section 4.1.

Appendix B Systematic Errors from Mass Rescaling

We consider an alternative version of our reference cluster sample, obtained by merging KiDS, WHL, and DESI only after imposing the lower mass cut $M_{500} > 10^{14} M_{\odot}$, but without applying any mass rescaling to WHL and DESI. We remove cluster repetitions by following the same process as set out in Section 3.5, i.e., we always keep the KiDS clusters, but for the remaining repetitions between WHL and DESI, we randomly choose one to discard. In the end, KiDS, WHL, and DESI contribute 806, 15,114, and 9,684 clusters, respectively, for a total of 25,604 clusters spanning the redshift range $0.02 < z < 0.97$ and the mass range $14.0 < \log(M_{500}/M_{\odot}) < 15.2$. The cluster redshift and mass distributions are qualitatively similar

to the ones shown in Figure 6. We then split the clusters over the same set of $M-z$ bins as considered in our fiducial sample, and proceed with the measurements of the stacked signal, the angular profiles, and the covariance matrices, following the same methodology as described in Section 4.2. We do not include plots of the resulting stacks and correlation matrices, as they are similar to the ones that we have already shown for our fiducial sample. Instead, we show comparisons between the measured profiles and the ones from the fiducial sample for Planck in Figure 16 and for ACT in Figure 17. We notice that for the lowest-redshift bin, there is a clear offset in the profile amplitude; this difference is practically negligible for the highest-redshift bin, which is mostly dominated by DESI clusters that (for $z > 0.80$) did not undergo any explicit mass rescaling. In general, the difference is also quite mild for the marginalized cases, with the profiles obtained from the full samples showing compatibility over the whole θ range.

As noted in Section 6.1, we also perform our MCMC parameter estimation on this new set of unscaled profiles. The resulting contours are plotted in Figures 18–22, for all $M-z$ bins. These plots are also used to show the posterior distributions that were obtained with our fiducial sample; given the large number of resulting contours, we include them here in order to keep the main text of the paper lighter. As already discussed in Section 6.3, the contours that are obtained from the unscaled sample generally resemble the ones that are obtained from the fiducial sample; any systematic errors deriving from our mass rescaling are then of second order compared to the final statistical errors that are obtained on the parameters, which are in turn mostly driven by the degeneracy of the model.

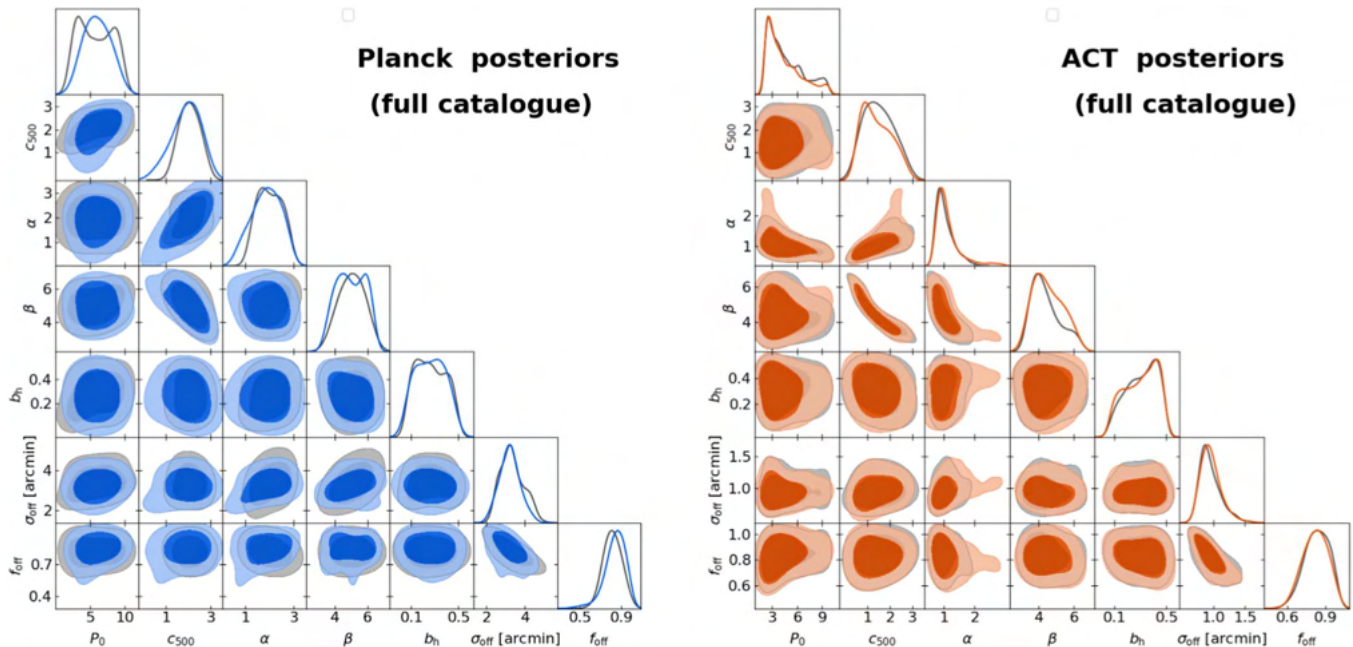


Figure 18. Comparison between the final posteriors (plotted as contours showing the 68% and 95% confidence levels) obtained using the cluster sample with and without mass rescaling, for the cases of Planck (left) and ACT (right). The colored contours are obtained from the mass-rescaled catalog, and are the same as the ones shown in Figure 12. The gray contours are derived from the catalog obtained with no mass rescaling.

Planck posteriors (independent M-z bins)

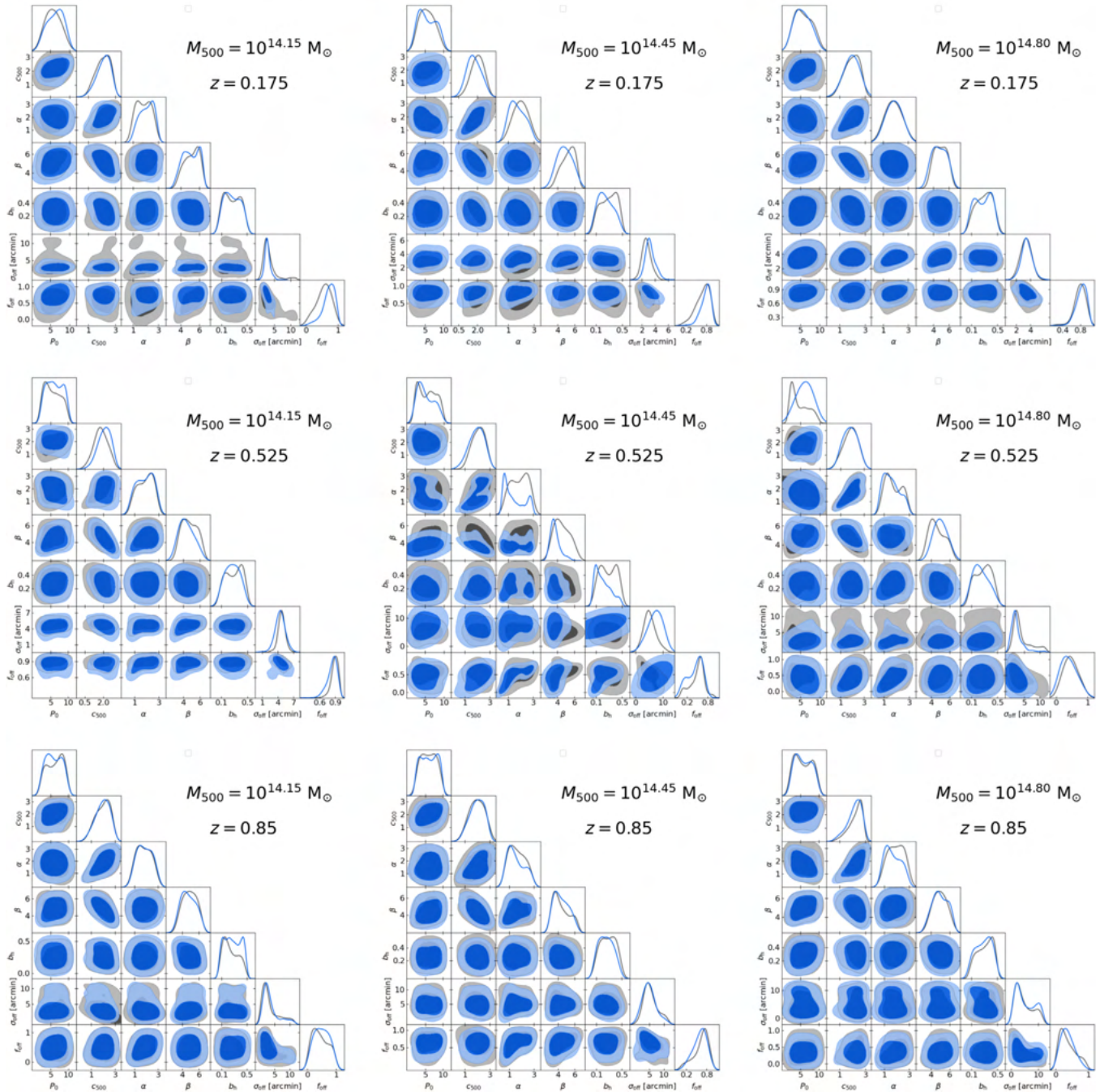


Figure 19. Planck posterior distributions (with the contours showing the 68% and 95% confidence levels) on the fitted parameters for each independent M - z bin, obtained from the mass-rescaled catalog (blue) and the one with no mass rescaling (gray).

Planck posteriors (marginalized bins)

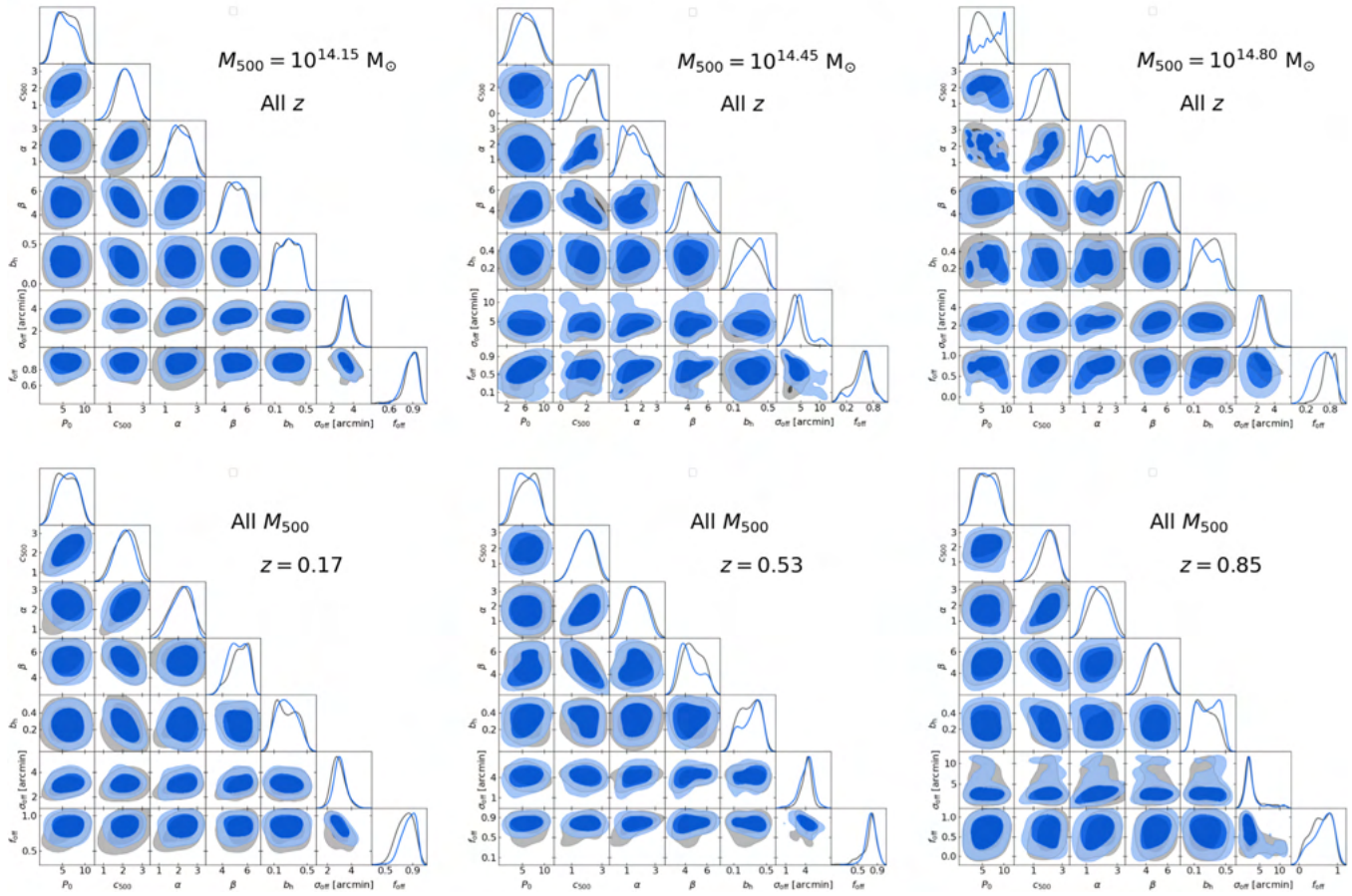


Figure 20. The same as Figure 19, but this time showing the bins marginalized over M_{500} or z .

ACT posteriors (independent M-z bins)

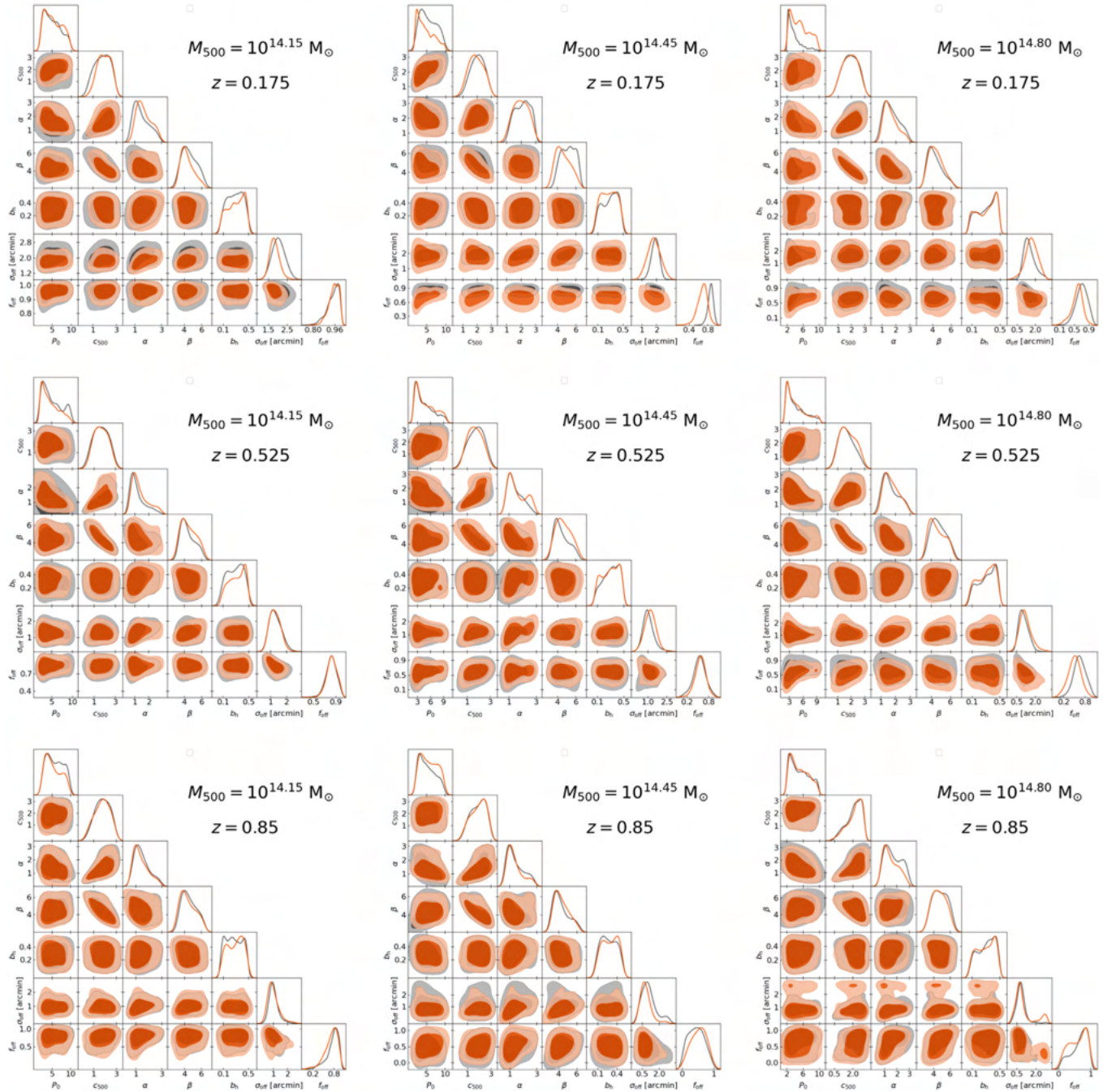


Figure 21. ACT posterior distributions (with the contours showing the 68% and 95% confidence levels) on the fitted parameters for each independent M - z bin, obtained from the mass-rescaled catalog (red) and the one with no mass rescaling (gray).

ACT posteriors (marginalized bins)

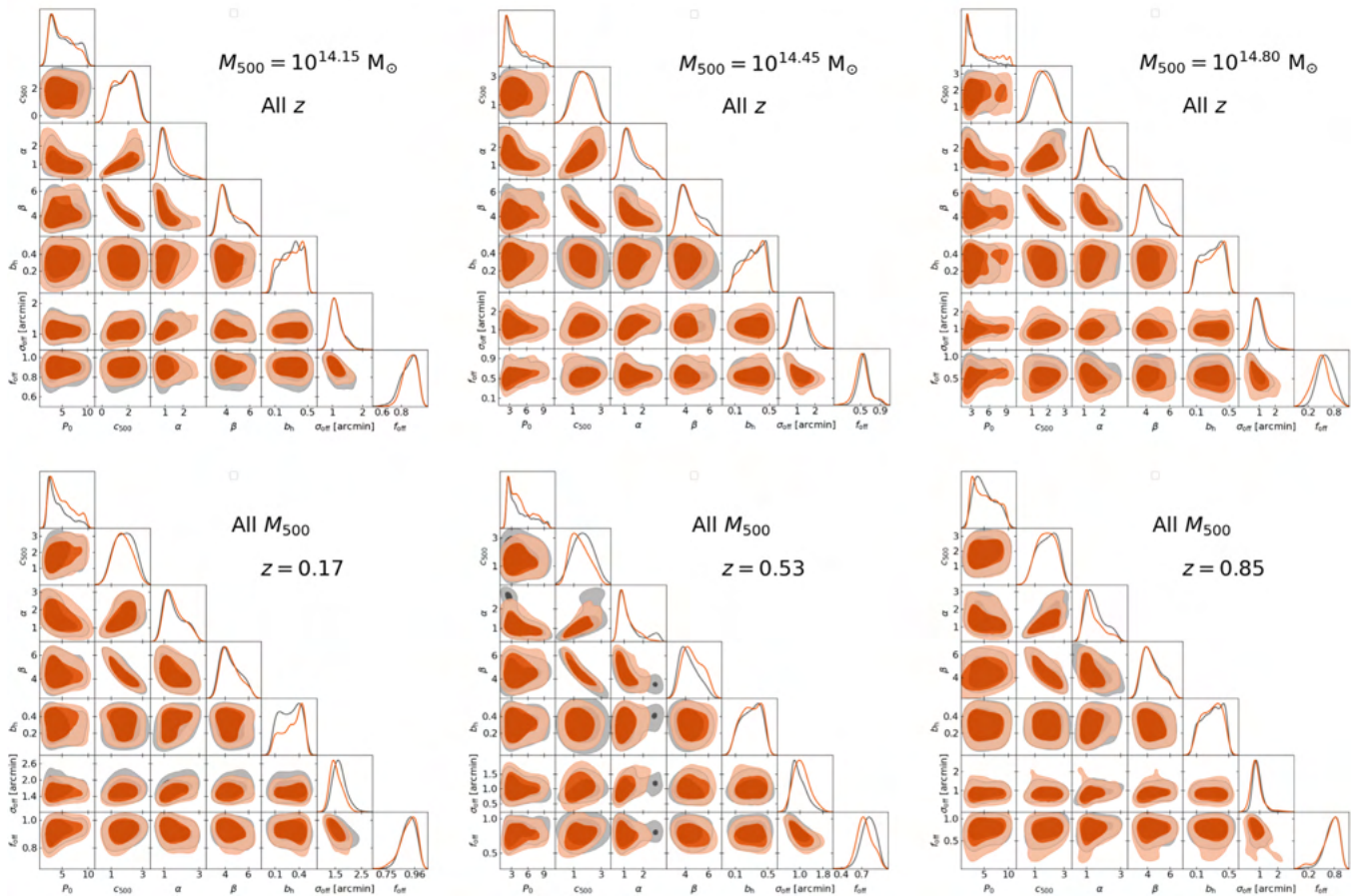


Figure 22. The same as Figure 21, but this time showing the bins marginalized over M_{500} or z .

ORCID iDs

Denis Tramonte <https://orcid.org/0000-0002-6754-1448>
 Yin-Zhe Ma <https://orcid.org/0000-0001-8108-0986>
 Ziang Yan <https://orcid.org/0000-0001-8043-5378>
 Matteo Maturi <https://orcid.org/0000-0002-3517-2422>
 Gianluca Castignani <https://orcid.org/0000-0001-6831-0687>
 Mauro Sereno <https://orcid.org/0000-0003-0302-0325>
 Sandro Bardelli <https://orcid.org/0000-0002-8900-0298>
 Carlo Giocoli <https://orcid.org/0000-0002-9590-7961>
 Federico Marulli <https://orcid.org/0000-0002-8850-0303>
 Lauro Moscardini <https://orcid.org/0000-0002-3473-6716>
 Emanuela Puddu <https://orcid.org/0000-0002-4522-6164>
 Mario Radovich <https://orcid.org/0000-0002-3585-866X>
 Ludovic Van Waerbeke <https://orcid.org/0000-0002-2637-8728>
 Angus H. Wright <https://orcid.org/0000-0001-7363-7932>

References

Aghanim, N., Douspis, M., Hurier, G., et al. 2019, *A&A*, 632, A47
 Aguado-Barahona, A., Rubiño-Martín, J. A., Ferragamo, A., et al. 2022, *A&A*, 659, A126
 Aihara, H., Allende Prieto, C., An, D., et al. 2011, *ApJS*, 193, 29
 Alam, S., Albareti, F. D., Allende Prieto, C., et al. 2015, *ApJS*, 219, 12
 Allen, S. W., Evrard, A. E., & Mantz, A. B. 2011, *ARA&A*, 49, 409
 Arnaud, M., Pratt, G. W., Piffaretti, R., et al. 2010, *A&A*, 517, A92
 Barnes, D. J., Vogelsberger, M., Pearce, F. A., et al. 2021, *MNRAS*, 506, 2533
 Battaglia, N., Bond, J. R., Pfrommer, C., & Sievers, J. L. 2012, *ApJ*, 758, 75

Bellagamba, F., Roncarelli, M., Maturi, M., & Moscardini, L. 2018, *MNRAS*, 473, 5221
 Bellagamba, F., Sereno, M., Roncarelli, M., et al. 2019, *MNRAS*, 484, 1598
 Birkinshaw, M. 1999, *PhR*, 310, 97
 Bleem, L. E., Bocquet, S., Stalder, B., et al. 2020, *ApJS*, 247, 25
 Böhringer, H., Schuecker, P., Pratt, G. W., et al. 2007, *A&A*, 469, 363
 Carlstrom, J. E., Holder, G. P., & Reese, E. D. 2002, *ARA&A*, 40, 643
 Czakon, N. G., Sayers, J., Mantz, A., et al. 2015, *ApJ*, 806, 18
 Davis, M., Efstathiou, G., Frenk, C. S., & White, S. D. M. 1985, *ApJ*, 292, 371
 de Jong, J. T. A., Verdoes Kleijn, G. A., Erben, T., et al. 2017, *A&A*, 604, A134
 Dey, A., Schlegel, D. J., Lang, D., et al. 2019, *AJ*, 157, 168
 Fang, W., Kadota, K., & Takada, M. 2012, *PhRvD*, 85, 023007
 Ferragamo, A., Barrena, R., Rubiño-Martín, J. A., et al. 2021, *A&A*, 655, A115
 Giocoli, C., Marulli, F., Moscardini, L., et al. 2021, *A&A*, 653, A19
 Gong, Y., Ma, Y.-Z., & Tanimura, H. 2019, *MNRAS*, 486, 4904
 Goodman, J., & Weare, J. 2010, *CAMCS*, 5, 65
 Górski, K. M., Hivon, E., Banday, A. J., et al. 2005, *ApJ*, 622, 759
 Hartlap, J., Simon, P., & Schneider, P. 2007, *A&A*, 464, 399
 Hasselfield, M., Hilton, M., Marriage, T. A., et al. 2013, *JCAP*, 2013, 008
 He, Y., Mansfield, P., Rau, M. M., Trac, H., & Battaglia, N. 2021, *ApJ*, 908, 91
 Hicks, A. K., Ellingson, E., Bautz, M., et al. 2008, *ApJ*, 680, 1022
 Hilton, M., Sifón, C., Naess, S., et al. 2021, *ApJS*, 253, 3
 Hoekstra, H., Herbonnet, R., Muzzin, A., et al. 2015, *MNRAS*, 449, 685
 Hojjati, A., McCarthy, I. G., Harnois-Déraps, J., et al. 2015, *JCAP*, 2015, 047
 Hojjati, A., Tröster, T., Harnois-Déraps, J., et al. 2017, *MNRAS*, 471, 1565
 Hurier, G., Macías-Pérez, J. F., & Hildebrandt, S. 2013, *A&A*, 558, A118
 Ibitoye, A., Tramonte, D., Ma, Y.-Z., & Dai, W.-M. 2022, *ApJ*, 935, 181
 Ishiyama, T., Prada, F., Klypin, A. A., et al. 2021, *MNRAS*, 506, 4210
 Joachimi, B., Lin, C. A., Asgari, M., et al. 2021, *A&A*, 646, A129
 Johnston, D. E., Sheldon, E. S., Wechsler, R. H., et al. 2007, arXiv:0709.1159
 Klein, M., Oguri, M., Mohr, J. J., et al. 2022, *A&A*, 661, A4
 Komatsu, E., & Kitayama, T. 1999, *ApJL*, 526, L1

- Le Brun, A. M. C., McCarthy, I. G., & Melin, J.-B. 2015, *MNRAS*, **451**, 3868
- Ma, Y.-Z., Gong, Y., Tröster, T., & Van Waerbeke, L. 2021, *MNRAS*, **500**, 1806
- Madhavacheril, M. S., Hill, J. C., Naess, S., et al. 2020, *PhRvD*, **102**, 023534
- Makiya, R., Hikage, C., & Komatsu, E. 2020, *PASJ*, **72**, 26
- Mantz, A., Allen, S. W., Ebeling, H., Rapetti, D., & Drlica-Wagner, A. 2010, *MNRAS*, **406**, 1773
- Maturi, M., Bellagamba, F., Radovich, M., et al. 2019, *MNRAS*, **485**, 498
- Mehrtens, N., Romer, A. K., Hilton, M., et al. 2012, *MNRAS*, **423**, 1024
- Nagai, D., Kravtsov, A. V., & Vikhlinin, A. 2007, *ApJ*, **668**, 1
- Navarro, J. F., Frenk, C. S., & White, S. D. M. 1997, *ApJ*, **490**, 493
- Pearce, F. A., Kay, S. T., Barnes, D. J., Bower, R. G., & Schaller, M. 2020, *MNRAS*, **491**, 1622
- Piffaretti, R., Arnaud, M., Pratt, G. W., Pointecouteau, E., & Melin, J. B. 2011, *A&A*, **534**, A109
- Planck Collaboration, Ade, P. A. R., Aghanim, N., et al. 2011a, *A&A*, **536**, A8
- Planck Collaboration, Ade, P. A. R., Aghanim, N., et al. 2011b, *A&A*, **536**, A11
- Planck Collaboration, Ade, P. A. R., Aghanim, N., et al. 2013, *A&A*, **550**, A131
- Planck Collaboration, Ade, P. A. R., Aghanim, N., et al. 2016a, *A&A*, **594**, A27
- Planck Collaboration, Aghanim, N., Arnaud, M., et al. 2016b, *A&A*, **594**, A22
- Planck Collaboration, Aghanim, N., Akrami, Y., et al. 2020, *A&A*, **641**, A6
- Pointecouteau, E., Santiago-Bautista, I., Douspis, M., et al. 2021, *A&A*, **651**, A73
- Remazeilles, M., Delabrouille, J., & Cardoso, J.-F. 2011, *MNRAS*, **410**, 2481
- Rotti, A., Bolliet, B., Chluba, J., & Remazeilles, M. 2021, *MNRAS*, **503**, 5310
- Sarazin, C. L. 1988, *S&T*, **76**, 639
- Sayers, J., Golwala, S. R., Ameglio, S., & Pierpaoli, E. 2011, *ApJ*, **728**, 39
- Sayers, J., Golwala, S. R., Mantz, A. B., et al. 2016, *ApJ*, **832**, 26
- Sereno, M., Covone, G., Izzo, L., et al. 2017, *MNRAS*, **472**, 1946
- Sunyaev, R. A., & Zeldovich, Y. B. 1972, *CoASP*, **4**, 173
- Takey, A., Schwobe, A., & Lamer, G. 2014, *A&A*, **564**, A54
- Tinker, J., Kravtsov, A. V., Klypin, A., et al. 2008, *ApJ*, **688**, 709
- Tinker, J. L., Robertson, B. E., Kravtsov, A. V., et al. 2010, *ApJ*, **724**, 878
- Vikhlinin, A., Burenin, R. A., Ebeling, H., et al. 2009, *ApJ*, **692**, 1033
- Voges, W., Aschenbach, B., Boller, T., et al. 1999, *A&A*, **349**, 389
- Voit, G. M. 2005, *RvMP*, **77**, 207
- von der Linden, A., Allen, M. T., Applegate, D. E., et al. 2014, *MNRAS*, **439**, 2
- Wang, H., Mo, H. J., Yang, X., et al. 2016, *ApJ*, **831**, 164
- Wen, Z. L., & Han, J. L. 2015, *ApJ*, **807**, 178
- Wen, Z. L., Han, J. L., & Liu, F. S. 2012, *ApJS*, **199**, 34
- Yan, Z., Raza, N., Van Waerbeke, L., et al. 2020, *MNRAS*, **493**, 1120
- Yang, X., Mo, H. J., van den Bosch, F. C., et al. 2006, *MNRAS*, **373**, 1159
- Yang, X., Mo, H. J., van den Bosch, F. C., et al. 2007, *ApJ*, **671**, 153
- Yang, X., Mo, H. J., van den Bosch, F. C., & Jing, Y. P. 2005, *MNRAS*, **356**, 1293
- Yang, X., Xu, H., He, M., et al. 2021, *ApJ*, **909**, 143